The effect of energetic electron precipitation on the nitric oxide density in the lower thermosphere

Camilla Sætre

Thesis for the degree of Philosophiae Doctor (PhD)

at the University of Bergen

December 2006

Preface

This PhD thesis is the result of three years work funded by the Research Council of Norway. The project was proposed by my supervisor Johan Stadsnes, who has many years experience on the field of energetic electron precipitation and X-ray imaging. Johan has been enthusiastic and helpful during these years, and for that I am most grateful. My second supervisor, Nikolai Østgaard, has also given me valuable comments and ideas, in addition to practical help with the data analysis. Thank you, both.

During the PhD project, I spent three months at the Laboratory for Atmospheric and Space Physics, LASP, in Boulder Colorado. Here I worked together with Dr Charles Barth, who is one of the great pioneers and experts on the nitric oxide chemistry in the upper atmosphere. I would like to thank him, and his colleagues Dr Daniel Baker and Dr Scott Bailey, who also have been involved in the SNOE project. I also thank Dr Glynn Germany and Dr Jesper Gjerloev for providing data.

These last years would not nearly have been as fun if it had not been for the fantastic space physics group here at the institute. I have enjoyed many discussions, seminars, and coffee breaks together with my fellow students and colleagues. I especially want to thank Marit Sandanger and Marita Sørbø, who I had the pleasure of shearing office with.

Finally I send a huge gratitude to my family and friends, especially Jan-Tore. Thank you for all support and encouragement.

Bergen, December 2006 Camilla Sætre

Contents

Chapter 1

Introduction

Courtesy of Jan Curtis

The objective of this thesis has been the study of the chemical effects of the electron precipitation in the upper atmosphere, and mainly the increase of thermospheric nitric oxide (NO). NO plays an important role in the temperature balance for the mesosphere and thermosphere. Nitric oxide molecules have a relatively low ionization threshold (9.26 eV), and NO^+ is one of the main ion constituents in the lower part of the ionosphere. In addition nitric oxides are able to destroy ozone in a catalytic reaction. The lifetime of NO is $\sim$1 day.

Nitric oxide in the lower thermosphere is primarily formed when atomic nitrogen reacts with molecular oxygen. Dissociation of N_2 by energetic electrons is an important source of N atoms. In addition N_2^+ ions will produce atomic nitrogen when reacting with O atoms or via recombination. Below $\sim$130 km altitude the production of NO is mainly from excited nitrogen, and ground state nitrogen will in addition to creating NO also destroy it. The dissociation and ionization processes are caused by energetic electrons, both photoelectrons caused by solar radiation, and more efficiently the energetic auroral electrons.

Numerous studies of daily averaged NO densities show a distinct connection between enhanced density of thermospheric nitric oxide at higher latitudes and auroral activity (e.g. *Barth*, 1992; *Petrinec et al.*, 2003). The work presented in this thesis, is the first to compare directly the development of enhanced NO densities and the auroral energy input. This is done for the beginning of geomagnetic storms, where the geomagnetic conditions up to one day prior to the observations were relatively quiet.

In this project auroral electron precipitation data, derived from the Polar Ionospheric X-ray Imaging Experiment (PIXIE) and the Ultraviolet Imager (UVI) on board the Polar satellite, have been used together with NO density measurements from the Student Nitric Oxide Explorer (SNOE). A photochemical NO_x-model has been used to infer the auroral energy flux from the SNOE nitric oxide measurements (*Barth*, 1992; *Bailey et al.*, 2002). This model has also been used for nitric oxide calculations with auroral energy input derived from PIXIE and UVI measurements, and from SuperMAG geomagnetic index parametrizations. The results were compared with SNOE nitric oxide data.

In the first part of this thesis the theoretical background for the nitric oxide chemistry is presented, along with an overview of some of the previous studies done on this topic. The methods and instruments used in this PhD study are also introduced, and finally a summary of the papers is given. The second part of the thesis consists of the three following papers:

Paper I: C. Sætre, J. Stadsnes, H. Nesse, A. Aksnes, S. M. Petrinec, C. A. Barth, D. N. Baker, R. R. Vondrak and N. Østgaard (2004). Energetic electron precipitation and the NO abundance in the upper atmosphere: A direct comparison during a geomagnetic storm, *J. Geohpys. Res., 109*, A09302, doi:10.1029/2004JA010485.

Paper II: C. Sætre, C. A. Barth, J. Stadsnes, N. Østgaard, S. M. Bailey, D. N. Baker and J. W. Gjerloev (2006). Comparisons of electron energy deposition derived from observations of lower thermospheric nitric oxide and from X-ray bremsstrahlung measurements. *J. Geohpys. Res., 111*, A04302, doi:10.1029/2005JA011391.

Paper III: C. Sætre, C. A. Barth, J. Stadsnes, N. Østgaard, S. M. Bailey, D. N. Baker, G. A. Germany and J. W. Gjerloev (2006). Thermospheric nitric oxide at higher latitudes - Model calculations with auroral energy input, *Submitted to Journal of Geophysical Research.*

Chapter 2

Theory and background

The basic chemistry for nitric oxide in the upper atmosphere is presented here. A short review is then given of the different observations for the last decades of the thermospheric nitric oxide density. The observations are based on different measurement techniques. There is also given a brief summary of various chemical models for nitric oxides. Primarily the previous versions of the photochemical NO_x model used in Paper II and Paper III of the thesis, are presented.

2.1 Chemistry of nitric oxide in the upper atmosphere

The importance of NO was first recognized indirectly by discovering the importance of NO^+ for the D-region of the ionosphere, which was ascertained already in the 1940's. The solar X-ray and extreme ultraviolet (EUV) radiation, capable of ionizing the major atmospheric constituents, are absorbed above ~100 km altitude. Solar Lyman-alpha radiation is able to penetrate the absorbing molecular oxygen layers, and get deep enough to ionize NO molecules forming the D-layer of the ionosphere. The ionization threshold for NO (9.26 eV) is low enough to make this possible, and NO^+ is one of the major constituents of the ionosphere. Variations in the NO density will cause direct variations in the D-region electron density. Also in the E and F_1 regions of the ionosphere, NO is important for several ion-molecule and charge exchange reactions. Figure 2.1 shows the densities for the main atmospheric constituents, nitric oxide density between 90 and 170 km altitude, and the electron density and ion densities in the ionosphere as a function of altitude (units of cm^{-3}). Also shown is the temperature profile of the atmosphere, and the regions known as the thermosphere (from 90 km to ~400 km), mesosphere (between 50 and 90 km), and stratosphere (between ~10 and 50 km).

Nitric oxide also influences the temperature of the upper atmosphere. As a heteronuclear molecule NO radiates effectively infrared radiation at 5.3 μm, causing a cooling of the atmosphere. Observations of the rotational structure of the fluorescence emissions of NO can be used to derive the temperature profiles of the lower thermosphere (*Barth and Eparvier*, 1993). This is done by generating synthetic spectra of the NO gamma bands,

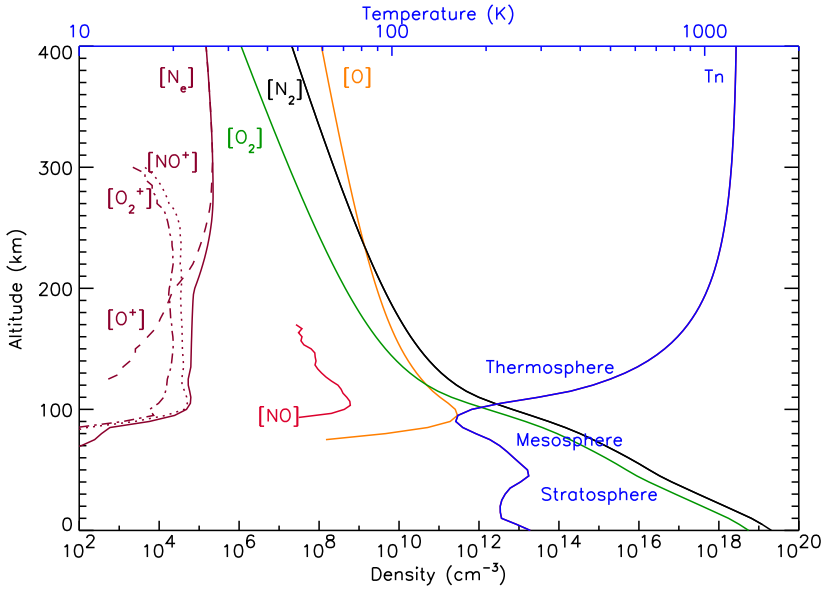

Figure 2.1: Main atmospheric constituents (N_2, O_2, and O), and the neutral temperature (Tn) as a function of altitude (from MSIS model). Also shown are the electron density (N_e) of the ionosphere, and the density of some of the most important ions (O_2^+, NO^+, and O^+, night values from the IRI model), and the nitric oxide density between 90 and 170 km altitude (from SNOE measurements).

and do a multiple linear regression analysis of the measured and the synthetic spectra. The rotational structure of the NO dayglow emission bands is highly dependent on the atmospheric temperature. For higher temperatures the rotational bands are wider with a lower amplitude. In the lower thermosphere the collision frequency is large enough that one can assume the NO molecule to be in rotational equilibrium with the ambient atmosphere. That means, the temperature derived from the NO emission bands equals the neutral temperature of the atmosphere. The measured emission spectra must be divided in altitude bins sufficiently large to give a high signal-to-noise ratio. The spectral resolution for the rocket measurements in the work of *Barth and Eparvier* (1993) was 0.2 nm, and the temperature steps of the synthetic spectra were of 10°K. Their results were a temperature profile that varied from 280°K at 110 km to 700°K at 140 km.

Nitric oxide has maximum density in the lower thermosphere at ∼105-110 km altitude. NO is produced when energetic electrons, solar X-rays and extreme ultraviolet (EUV) dissociate, excite and ionize the neutral gas in the atmosphere. The balance between the energy deposition and hence the production of NO, and the loss processes for NO, decides the altitude of maximum NO density. The most important source of NO is excited atomic nitrogen, N(^{2}D), in reaction with molecular oxygen (reaction 2.1). This process is most efficient at ∼105 km altitude.

$$N(^2D) + O_2 \rightarrow NO + O \tag{2.1}$$

The same process, only with ground state atomic nitrogen, N(^{4}S), instead of excited, is also important for NO production (reaction 2.2). This reaction however, is highly temperature dependent, and only becomes important above ∼130 km altitude.

$$N(^4S) + O_2 \rightarrow NO + O \tag{2.2}$$

$$NO + N(^4S) \rightarrow N_2 + O \tag{2.3}$$

Since reaction with N(^{4}S) works as an important loss for NO (reaction 2.3), with maximum efficiency at ∼105 km altitude, the NO abundance in the lower thermosphere is determined by the ratio of excited to ground state atomic nitrogen.

The NO density production from auroral energetic electrons, can be more than one order of magnitude greater than that produced at middle to lower latitudes by photoelectrons from solar soft X-rays and solar EUV radiation. Joule and particle heating will also give more production of NO, as the temperature dependent reaction of N(^{4}S) with O_2 will be more efficient the warmer it is. This effect is more important at altitudes above the main region for auroral energy deposition (i.e. ∼150 km). Vertical winds and diffusion can transport these increased amounts of NO downward to ∼110 km altitude. Simultaneous horizontal transport can then give more NO density in the regions south and north of the auroral oval.

The most important loss mechanism for NO is photodissociation by solar far ultraviolet radiation (FUV) (reaction 2.4). In this process N(^{4}S) is produced, which can react with another NO molecule and give the end product N_2 (reaction 2.3). The effective lifetime of NO due to this reduction process is 19.6 hours (*Minschwaner and Siskind*, 1993).

$$NO + h\nu \rightarrow N(^4S) + O \tag{2.4}$$

The long lifetime of NO (∼1 day) makes it a useful trace gas for atmospheric motion in the lower thermosphere. For example the NO density can be used to detect gravity waves.

If the NO_x (NO and NO_2 mainly) is located at higher latitudes in polar winter, the lifetime of the NO_x gas can be much longer than one day due to the absence of photodissociation by solar FUV. There is a meteorological phenomenon called the winter polar vortex, which may confine the NO_x gas within the polar regions. The strong cooling due to lack of insolation in the polar regions during winter, drives a vortex separating the high latitude air from the solar illuminated lower latitude air outside the vortex. The NO_x gas produced in the lower thermosphere and mesosphere by energetic electron precipitation, can live long enough if situated within a strong, persistent polar vortex lasting up to several months, to be transported down to the stratosphere. Here the NO molecules can react with ozone in a catalytic process where the NO molecule is not lost (reactions 2.5 and 2.6). This indirect effect of electron precipitation has been documented by e.g. *Callis et al.* (2001); *Randall et al.* (2001, 2005, 2006); *Siskind et al.* (2000).

$$NO + O_3 \rightarrow NO_2 + O \tag{2.5}$$

$$NO_2 + O \rightarrow NO + O_2 \tag{2.6}$$

In the work of *Randall et al.* (2005) observations from multiple spacecrafts showed a strong increase of stratospheric NO_x in the spring of 2004, and a concurrent pronounced decrease of stratospheric ozone. The increased NO_x values could be due to the very strong solar proton events late fall of 2003, and/or the strong polar vortex and energetic particle precipitation during the winter of 2004. With the datasets available, it was not possible though to distinguish the effects from the two processes.

The following study of *Randall et al.* (2006), showed the importance of a strong, persistent polar vortex for the descent of NO_x rich thermospheric and mesospheric air down to the stratosphere. In the spring of 2006, observations showed increase of NO_x mixing ratios north of 50°N from the mesosphere down to the stratosphere (see Figure 2.2). The energetic particle precipitation the fall and winter of 2005/2006, was quite low. In fact, the activity level was higher the winter season of 2004/2005. The observations, however, showed no signs of NO_x increase below the mesosphere the spring of 2005. Whereas for both spring 2004 and spring 2006, the NO_x increase was evident, throughout the mesosphere and down in the stratosphere. The results of *Randall et al.* (2006) confirmed that the impacts of energetic particle precipitation on the NO_x production in the upper atmosphere, and the following descent down to the stratosphere, are modulated by the meteorological conditions above the polar regions.

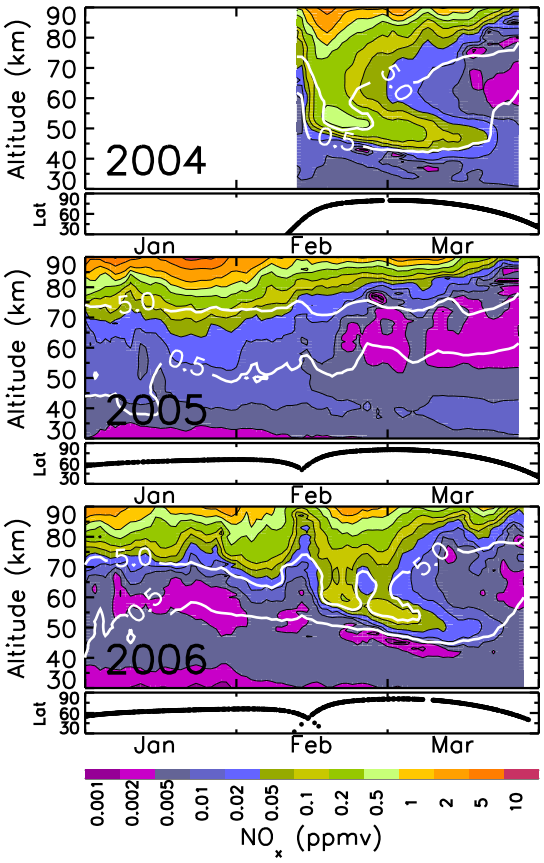

Figure 2.2: Atmospheric Chemistry Experiment (ACE) NO_x mixing ratios poleward of 50°N in (top) 2004, (middle) 2005, and (bottom) 2006. Also shown are the ACE occultation latitudes. White contours show ACE CO mixing ratios (ppmv). The figure is from *Randall et al.* (2006).

The nitric oxide concentration in the lower thermosphere, is affected by atmospheric heating and a following atmospheric expansion. In the regions of Joule heating, air that is rich in the molecular species is brought up from low in the atmosphere (*Burns et al.*, 2006). When the O/O_2 or O/N_2 ratio decrease, there will be better terms for the dissociation of N_2, and the following reaction between atomic nitrogen and O_2. In addition it is less opportunity for $N(^2D)$ to be quenched by atomic oxygen, instead of reacting with O_2 to form NO. Thus, atmospheric heating, causing a reduction in the atom-to-molecule ratio in the mesosphere and thermosphere, will favor the production of nitric oxide. This expansion

of the atmosphere due to heating, will naturally give an increased upward vertical neutral wind (*Hays et al.*, 1973). In addition there will be enhanced horizontal winds from ion-neutral coupling, driving the neutral constituents in a convection pattern that is similar to that of the ions (e.g. *Killeen et al.*, 1988). The transport of the NO gas may give a relative reduction of the NO density at the typical altitude and location for maximum density.

2.2 Observations of nitric oxide

The distribution of NO has been measured by several rocket and satellite experiments. The observations have mainly been either based on occultation experiments or emission experiments. The occultation method is to determine the NO density from the amount of absorption of sunlight in the atmosphere at sunset or sunrise. In the emission experiments the NO density is decided from the intensity of fluorescence emission from the molecule itself. The analysis of nitric oxide fluorescence requires adjustments of the data due to the Rayleigh scattering contribution to the fluorescence signal, and effects of self-absorption along the path through the atmosphere.

The Orbiting Geophysical Observatory (OGO-4) was the first satellite to observe thermospheric nitric oxide in 1968. The measurements were done with a nadir-viewing ultraviolet spectrometer, observing the fluorescence of NO molecules by solar radiation. The observations were primarily twilight measurements, between 37° and 85° latitude on either side of the equator. *Rusch and Barth* (1975) found from the OGO-4 measurements, that the NO density was higher in the polar regions. However, the higher values were not restricted to the auroral oval but extended poleward and equatorward. They also saw that the NO concentration varied as a function of time.

Gerard and Barth (1977) used high latitude observations of NO from the OGO-4 satellite, and a time-dependent model for calculation of the electron precipitation impact on the NO density. The NO density was derived from the (1,0) NO gamma band emissions, observed in regions of morning and evening twilight. The model calculated the ionization and dissociation by energetic electron precipitation, and the subsequent production of NO. The intensity of the auroral electrons was derived from O_I λ135.6 nm auroral emissions. The calculated NO density was found to gradually build up during the strong auroral activity, to a factor 4 more than prior to the storm. The calculated NO densities were comparable to those measured by the OGO satellite. In the recovery phase the NO density decreased slowly. When comparing the measured NO density with the observed instantaneous auroral brightness, they found no direct relationship. The result of the study was that the observed increase in thermospheric NO during auroral activity, was primarily due to ionization by precipitating energetic electrons.

The Atmosphere Explorer (AE) satellites were the first to measure the fluorescence of NO by limb scanning (*Barth et al.*, 1973). AE-C had a 68° inclination of the orbit, and was operating from December 1973 until December 1978. *Cravens and Stewart* (1978) analyzed the AE-C NO measurements at 105 km altitude, and found that the lower E-region NO density depended on latitude, longitude and geomagnetic activity. They found

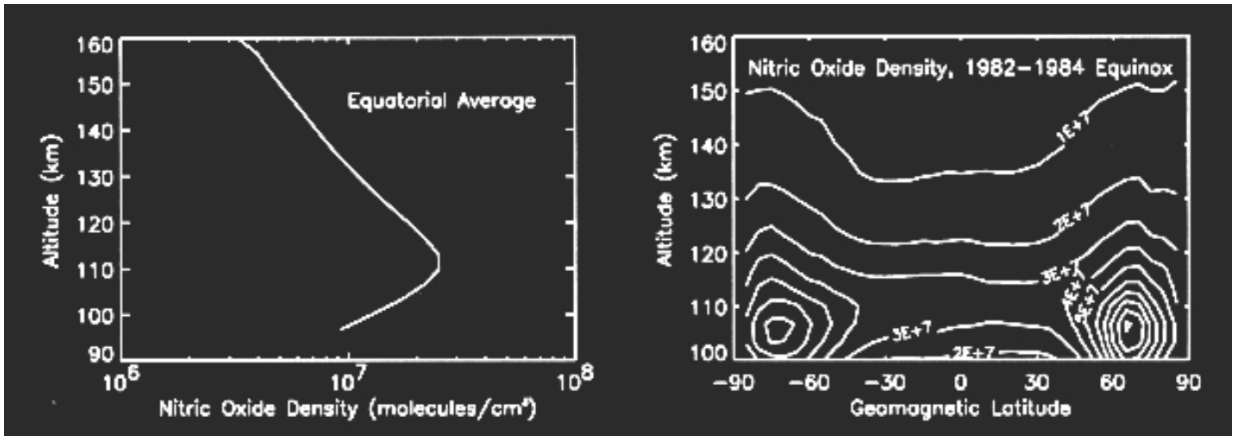

Figure 2.3: Nitric oxide density measured by the Solar Mesosphere Explorer. Average equinox values for the period 1982-1984. (Figure from the SME website.)

that even low latitude NO density increased slightly during major geomagnetic storms. It was also found an asymmetry about the magnetic pole, which they hypothesized, was due to horizontal transport of NO from the auroral zone by thermospheric winds. AE-D also measured the thermospheric NO density. It was in a polar orbit in the short time range from October 1975 until January 1976. *Cravens et al.* (1985) analyzed the nitric oxide data from AE-D. They confirmed the NO density variations with latitude and level of geomagnetic activity, as previously observed by AE-C at 105 km altitude. In addition they found the shape of the NO altitude profile and how it varied with latitude. Even for average magnetic activity conditions, they saw a substantial latitudinal gradient of NO in the lower thermosphere from the lower to the higher latitudes. This was especially strong in the winter hemisphere.

The Solar Mesosphere Explorer (SME) had a Sun-synchronous orbit with a local time of ∼1500, and measured NO fluorescent scattering by limb-scanning with an ultraviolet spectrometer. Measurements at all latitudes of the NO density as a function of altitude (95-160 km), were made over a four and a half year period from January 1982 until August 1986 (*Barth*, 1992). The observations were made on only one or two orbits per day, and thus global measurements of the daily NO distribution were not obtained on a daily basis. Figure 2.3 shows an example of the NO measurements from SME. On the left, is the altitude profile for equatorial average density, showing a maximum NO value at 110 km. On the right is a contour plot of the average NO density as a function of geographical latitude and altitude. Although it was for equinox values, the maximum NO density was $1 \times 10^8 [cm^{-3}]$ around 65°N, and $7 \times 10^7 [cm^{-3}]$ around 70°S.

The Halogen Occultation Experiment (HALOE) on board the Upper Atmosphere Research Satellite (UARS), measured the atmospheric temperature and composition, including vertical profiles of NO and NO_2, from October 1991 until November 2005 (*Russel et al.*, 1993). The technique used was limb observations of the occultation of sunlight by the different atmospheric constituents at sunrise and sunset. The latitudinal coverage

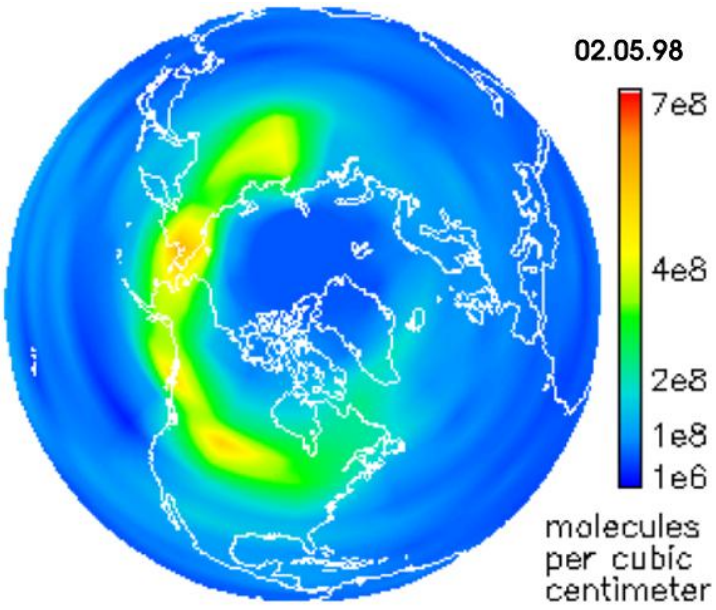

Figure 2.4: Nitric oxide density at 106 km altitude measured by the Student Nitric Oxide Explorer above the northern hemisphere. Interpolated over 15 orbits for 2 May, 1998.

varied from day to day. Due to the solar occultation technique many weeks of observations were required to provide extensive global coverage. The NO measurements derived from HALOE and SME were compared in *Siskind et al.* (1998). Both datasets showed a well defined decrease of NO during the decline of solar activity. The large NO abundance at higher and mid-latitudes were found to be connected to auroral activity. In addition HALOE observations showed that mesospheric nitric oxide increased during winter due to more downward transport of thermospheric NO, and less destruction of NO due to reduced photodissociation.

The Middle Atmosphere High Resolution Spectrograph Investigation (MAHRSI) observed the nitric oxide distribution from limb intensity profiles of the fluorescence of NO (*Stevens et al.*, 1997). The MAHRSI experiment was on board the ASTRO-SPAS (Shuttle Pallet Satellite) spacecraft, which was deployed and retrieved by the space shuttle. The observations were done during November 1994, following a period of intense geomagnetic activity. The altitude range was 76-140 km, and the data were seven hour snapshots of NO from sunrise at 48°S to sunset at 61°N for each orbit. Comparisons with coincident HALOE observations of NO suggested that the NO density in the lower thermosphere and mesosphere was strongly influenced by dynamics.

The polar orbiting Student Nitric Oxide Explorer (SNOE) made global measurements of nitric oxide in the thermosphere by limb-scanning of the fluorescence of NO by solar radiation. The NO density as a function of altitude, longitude and latitude from March 1998 until September 2000 was measured by an ultraviolet spectrometer. The northern hemispheric NO density at 106 km altitude, 2 May 1998, is displayed in Figure 2.4. The image was obtained from 15 dayside tracks of SNOE measurements. The maximum NO

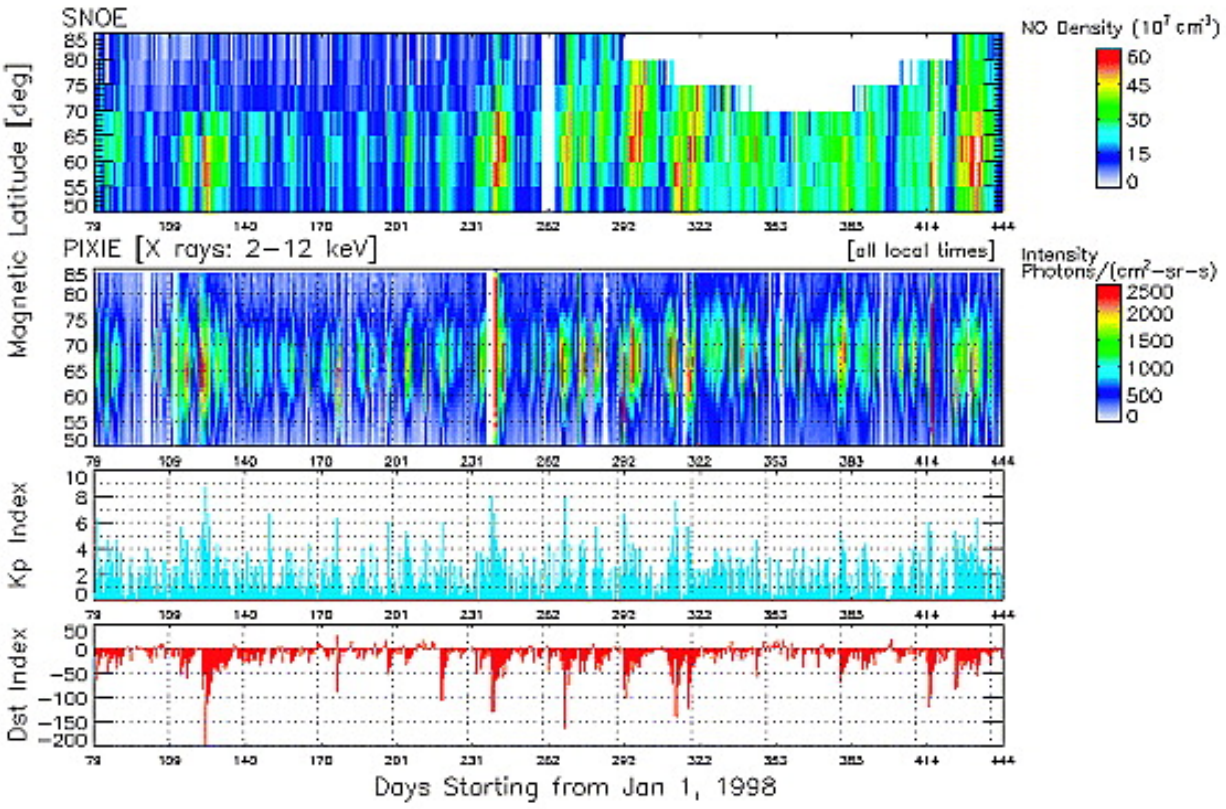

Figure 2.5: Keograms of SNOE nitric oxide measurements at 106 km altitude (top), and X-ray intensity from PIXIE's front chamber (second) in 1998. Northern hemisphere (50°N-85°N), daily averaged values, where the PIXIE data were averaged over all local times. The two lowest panels show the geomagnetic activity by the Kp index (blue) and the Dst index (red). The figure is from *Petrinec et al.* (2003).

density was clearly located in the region of the auroral oval. The SNOE experiment will be presented more thoroughly in the next chapter of Instruments and Techniques.

Petrinec et al. (2003) did a statistical study on the auroral variations of nitric oxide. They compared three years of data from SNOE nitric oxide observations, and the northern hemisphere X-ray bremsstrahlung observed by PIXIE. The daily averaged X-ray irradiance data and NO density at 106 km altitude, were also averaged over the geographic latitude range 50°-85° north. Figure 2.5 shows the variation of nitric oxide at 106 km altitude for the first year of the SNOE measurements, 1998, together with the variations of the auroral X-ray activity. The white areas are regions or time intervals without measurements. In the winter, the polar regions are not sunlit and SNOE was not able to measure the NO dayglow there. The X-ray bremsstrahlung were from the front chamber of the PIXIE camera (2-8 keV), and gave an indication of the intensity of the energetic electron precipitation. The figure also gives the geomagnetic activity (Kp and Dst indices) throughout the year, and one can see that the enhanced activity leads to the precipitation of energetic particles into the

auroral ionosphere, and also increased nitric oxide density in the lower thermosphere. Both strong and weak geomagnetic storms cause variations in the thermospheric NO density. The best correlation between the two datasets was found to be 0.6 when the SNOE data were delayed one day compared to the PIXIE X-ray observations. The one day lag is related to the auroral production of NO occurring at nighttime, whereas the SNOE observations took place on the dayside. *Petrinec et al.* (2003) stressed the difficulties of comparing two datasets where the timescales are that different. That is, the production and especially the loss for nitric oxide are much slower than the ionization and dissociation rates of the precipitating electrons, represented by the X-ray bremsstrahlung.

Barth et al. (1999) compared simultaneous measurements of the solar soft X-ray irradiance and the thermospheric nitric oxide density. Both measurements were daily averaged SNOE observations, for tropical latitudes and low geomagnetic activity (Ap < 10), both for the day of comparisons and for the previous day. The comparisons for 44 days during the spring of 1998 that met these criteria, showed a linear correlation between the two datasets of 0.88. This result confirmed the theory that the variation in the nitric oxide density for lower latitudes is controlled by the solar soft X-ray irradiance, at least for days with little auroral activity.

The work of *Baker et al.* (2001) investigated the relationship between precipitating energetic electrons and daily averaged nitric oxide densities in the lower thermosphere. They studied three geomagnetic storm events of 1998, and did a broader statistical study with daily averages of the NO density at 106 km altitude over two years (from March 1998 to March 2000). The NO densities were from SNOE measurements, and the auroral electron intensities were from Solar Anomalous and Magnetospheric Particle Explorer (SAMPEX) and also from National Oceanic and Atmospheric Research (NOAA) particle data. From the case studies they found that the electron count rates from SAMPEX were quite north-south symmetric between the two auroral zones. Whereas the nitric oxide densities showed much more north-south asymmetry. This was explained by the different amount of solar UV radiation for the different seasons, affecting the photodissociation of NO. The statistical study of daily averaged NO density from SNOE and the daily averaged electron count rate from SAMPEX, gave a correlation of 0.69. The correlation between the NO density and the NOAA hemispherical power index, was 0.63. The daily averages for the NO densities were not shifted one day later than the daily averaged electrons, as done in the work of *Petrinec et al.* (2003).

A new project for upper atmospheric research, is the Michelson Interferometer for Passive Atmospheric Sounding (MIPAS) on board ENVISAT. The satellite is polar-orbiting at an altitude of $\sim$800 km, and was launched in 2002. MIPAS is a Fourier transform spectrometer measuring earth limb emissions in the 4.15-14.6 μm range. This technique for NO density observations is quite different from the other techniques listed above. The model for retrieving the NO profiles from observations of the 5.3 μm emissions of NO rotational-vibrational states, is described in *Funke et al.* (2001). The method also works for non local-thermodynamic-equilibrium conditions.

2.3 Models for nitric oxides

Throughout the years, scientists have tried to model observed physical processes in order to understand them better. The processes of the Earth's ionosphere have been of interest for more than a century, since the first radio signal was transmitted across the Atlantic Ocean in 1901. The importance of nitric oxides to the ion and electron composition, especially in the lower part of the ionosphere, has urged the creation of chemical models for NO_x in the upper atmosphere.

The processes involving nitric oxides are best displayed by a photochemical model. Photochemistry is the interaction between atoms, small molecules and electromagnetic radiation, i.e. photons. *Cleary* (1986) developed a one-dimensional diffusive photochemical model for nitric oxide in the thermosphere. The NO density, deduced from rocket measurements of the γ, δ and ε dayglow emissions, was compared with the NO density calculated from the model. The model calculated the temporal variations of NO, $N(^4S)$, $N(^2D)$, NO^+, O_2^+, N_2^+, N^+, O^+ and $O(^2D)^+$ using the one-dimensional mass continuity equation,

$$\frac{\delta n_i}{\delta t} = P - Ln_i - \frac{\delta \phi_i}{\delta z} \tag{2.7}$$

Where n_i is the number density of the ith species, ϕ is the vertical flux including molecular and eddy diffusion, and P and L are the chemical production and loss terms. The vertical diffusion is only calculated for NO and $N(^4S)$. The chemical processes for the remaining species are fast enough to dominate the transport effects, and hence the last term of equation 2.7 can be set to zero. The time steps used in the model of *Cleary* (1986) were 15 minutes, except when the solar zenith angle was within 5° of sunrise or sunset, where the time steps were set to 5 minutes. This way one got higher accuracy during the periods of rapid changes in the densities. The solar parameters were updated at each time step. The calculation of the ionization rates was based on the work of *Torr et al.* (1979). The neutral atmosphere was calculated using the MSIS-83 model (*Hedin*, 1983) in one hour time steps. The photoelectron fluxes were calculated using the photoelectron model of *Strickland and Meier* (1982). With an estimated auroral energy flux of 0.5 ergs cm^{-2} sec^{-1} and a characteristic energy of 10 keV, the model NO density calculations were in good agreement with the measured NO density profile. The branching ratio for $N(^2D)/N(^4S)$ from the electron impact dissociation of N_2, was set to 0.6 in the work of *Cleary* (1986). This gave the best fit to the rocket observations below 120 km altitude. However, with different auroral parameters another branching ratio could give an equally good estimation of the NO density. The model showed increase in NO for increased auroral activity for branching ratios grater than 0.5 (*Rees and Roble*, 1979).

Siskind et al. (1989b,a) calculated the NO response to aurora using the same photochemical model as *Cleary* (1986), with some improvements. Instead of using MSIS, the background atmosphere was modeled using NCAR Thermospheric General Circulation Model (TGCM) (*Roble et al.*, 1988; *Richmond et al.*, 1992). Also the model input of solar energy was modified. The photoelectron model was still that of *Strickland and Meier* (1982). The model calculations of NO were compared to NO measurements from the Solar

Mesosphere Explorer (SME). *Siskind et al.* (1989b) compared the NO densities at low and middle latitudes. There was a good agreement between the observations and the calculations, implying that horizontal transport in the E-region of the ionosphere is not crucial for adequate calculation of lower thermospheric NO. The NO density was found to be larger at mid-latitudes than at the equator. This was thought to be due to the larger temperature increase at mid-latitudes from auroral activity. This heating of the atmosphere causes upwelling, and as a consequence of the global circulation a subsequent downwelling at lower latitudes (*Hays et al.*, 1973). The effect of downwelling is an increased atom-to-molecule ratio, and for upwelling a decrease. These changes will govern the reaction efficiency of $N(^4S)$ with O_2 to produce NO. Sensitivity tests showed that the low and mid-latitude NO density was much less sensitive to the value of the $N(^2D)$ yield from electron dissociation of N_2, than to either the O/O_2 ratio or the $N(^2D)$ quenching rate by atomic oxygen. *Siskind et al.* (1989a) compared model calculations of NO densities at auroral latitudes to that measured by the SME satellite. Since the NO gas in the lower thermosphere can take up to one day to build up and to decay, it is important to know the time history of the auroral activity in order to confidently model the NO response to a geomagnetic storm. *Siskind et al.* (1989a) used NOAA 6 and 7 particle measurements together with the Hemispherical Power Input (HPI) index, from the NOAA database, to derive a map of the energy input from energetic electron precipitation. The model calculations also included the effect on the NO density due to Joule heating through the calculations of the background atmospheric composition and temperature by the NCAR TGCM (*Roble et al.*, 1988; *Richmond et al.*, 1992). The photochemical model used the computer code of *Strickland et al.* (1976) to include the auroral electron energy input. The code calculated the energy degradation of an electron energy beam incident at the top of the atmosphere. The output of the code was electron energy flux as a function of altitude for energies from a few eV to tens of keV. This flux was used to calculate ionization and dissociation rates, with cross sections for the different processes as a function of electron energy. The time steps for the auroral energy input were 1 hour, and one assumed a maxwellian energy distribution. The comparisons to the SME observations showed that the calculated NO density greatly exceeded the measurements. The overestimate was too large to be explained by neither the lack of self-absorption adjustments of the SME data ($<30\%$ effect on [NO]), nor NOAA electron flux overestimation. Thus the uncertainties were assumed to lie within the NO chemistry of the model and possible dynamical loss processes. The conclusions were that there were two main explanations for the overestimation of NO from the model. One, that the yield of $N(^2D)$ may be less than 60-70% as used in the model. If it was reduced to 0.5, the modeled NO density at 110 km altitude was reduced by a factor of 2. Since the $N(^2D)$ yield is not a crucial parameter for the NO density at mid- and low latitudes, the better agreement between observations and model found in *Siskind et al.* (1989b) would not be affected by this change. Second explanation, is the effect of enhanced vertical advection due to upwelling caused by increased Joule heating. The vertical wind would have been able to transport large amounts of NO away from the production region at $\sim$110 km, during the period from the nighttime production to the time of SME observations ($\sim$1500LT).

Barth (1992) and *Bailey et al.* (2002) developed this photochemical model for thermo-

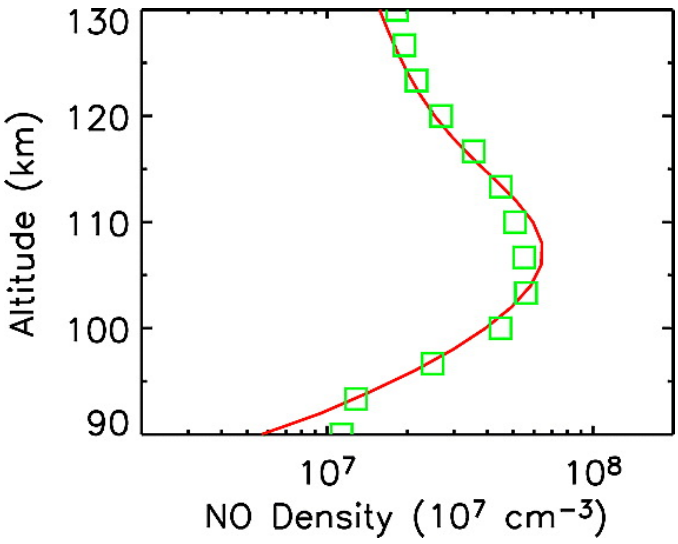

Figure 2.6: Model calculations (red) and SNOE observations (green) of the altitude variation of nitric oxide density for a 19-day average around 20 March 1998. The figure is from *Barth and Bailey* (2004).

spheric nitric oxides further. Their version of the model was used in the work of Papers II and III of this thesis, and the characteristics of this NO_x model version are elaborated on in the next chapter. In the work of *Barth and Bailey* (2004), the photochemical model was used to calculate the lower thermospheric NO density for a 935-day period, from March 1998 to September 2000. The result of the model was compared with the NO density measured by SNOE. As input to the model they used the observed solar soft X-ray irradiance (2-7 nm) from SNOE. The model did not include an energy input from the auroral electrons, and the comparisons were thus focused on lower latitudes ($<30°$) for relatively low auroral activity (Ap < 12). Figure 2.6 shows the model calculations (red) and the SNOE observations (green) of the NO density at the equator as a function of altitude. This was for spring equinox in 1998. The agreement was very good, considering the uncertainties of the measurements and of the model calculations. Figure 2.7 shows a scatter plot of the calculated NO density and the measured density. At 110 km altitude the correlation between the two datasets for periods of low auroral activity (Ap<12) was 0.88. These results showed that the photochemical model properly predicts the changes in the lower thermospheric NO densities as a result of daily changes in the solar soft X-ray irradiance (2-7 nm). The correlation between the model and the measurements for latitudes between 30°S and 30°N, was greater than 0.8 for all auroral activity levels (*Barth and Bailey*, 2004).

Dobbin et al. (2006) calculated the NO density in the lower thermosphere by use of a three-dimensional (3-D) Coupled Middle Atmosphere and Thermosphere (CMAT) general circulation model. The chemistry for this model was based on the same photochemical reactions as the model of *Bailey et al.* (2002). The thermospheric heating, photodissoci-

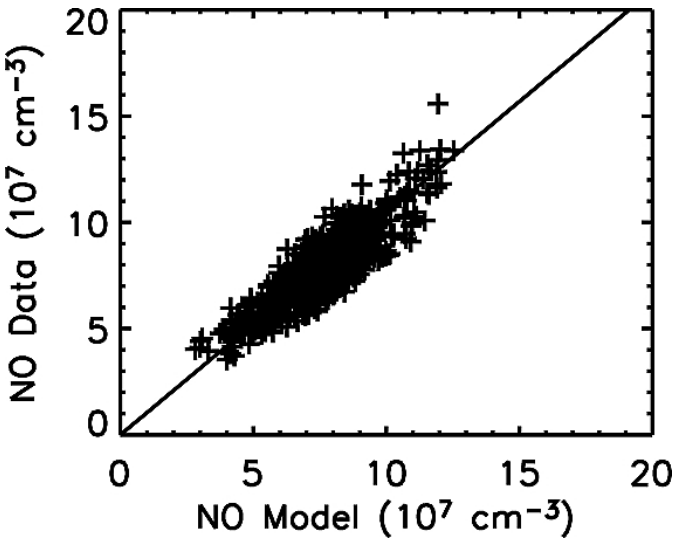

Figure 2.7: Correlation of model calculations and SNOE observations of equatorial nitric oxide density at 110 km. 568 days of low auroral activity (Ap<12). The solid line is a least-squares fit. The figure is from *Barth and Bailey* (2004).

ation, and photoionization from solar soft X-rays, EUV, and UV radiation (1.8-180 nm) were calculated using fluxes from the SOLAR2000 empirical model. The harder solar X-rays (0.2-1.8 nm) were from the *glow* model of *Solomon et al.* (1988); *Solomon and Abreu* (1989). The 3-D model also included auroral precipitation parameters from NOAA/TIROS statistical model for auroral precipitation (*Fuller-Rowell and Evans*, 1987; *Codrescu et al.*, 1997; *Foster et al.*, 1986), high latitude small-scale electric field variations (*Codrescu et al.*, 2000), and a global mean vertical eddy diffusion coefficient which was height dependent (*Garcia and Solomon*, 1983). The modeled NO density was compared with the NO density measured by SNOE. The comparisons showed that the 3-D model satisfactorily reproduced the temporal and spatial features of the zonal mean NO distribution under different geophysical conditions. The model, however, overestimated the higher latitude NO density by 30-50% at all altitudes.

There is also an empirical model of the nitric oxide in the upper atmosphere (100-150 km), the three dimensional Nitric Oxide Empirical Model (NOEM). This model is based on eigenvalue analysis of 2.5 years of NO measurements from the SNOE satellite (*Marsh et al.*, 2004). The three first empirical orthogonal functions (EOFs) were shown to vary with geomagnetic Kp index, solar declination, and the 10.7 cm solar flux. These three parameters are used as inputs to run the model. This empirical model can be used for validation of three-dimensional model calculations of thermospheric NO densities. The results from the empirical NO model can also in conjunction with general circulation models, test the stratospheric effects from thermospheric NO variations.

There are also several models for the neutral and ion chemistry specialized for the middle atmosphere, for example the Sodankylä Ion Chemistry model (*Verronen et al.*, 2002, and

references therein). This model includes the ionization from galactic cosmic radiation, and from proton precipitation, in addition to electron precipitation and solar UV radiation. This model calculates, among others, the nitric oxide density in the mesosphere. It does not include secondary electrons nor solar soft X-ray radiation, and neither any transport calculations.

The proton precipitation and cosmic radiation are not included in the NO_x photochemical model used in Paper II and III of this thesis. The average energy deposition from the proton precipitation is around 15% of the total energy deposition from particle precipitation (*Galand et al.*, 2001). Thus the protons are not considered to give a significant contribution to the nitric oxide density in the lower thermosphere.

2.4 NRLMSISE-00

The background neutral atmosphere for the NO_x photochemical model used here is from the NRL Mass Spectrometer, Incoherent Scatter radar Extended model, NRLMSISE-00 (*Picone et al.*, 2002). This model is an improvement of the MSISE-90 (*Hedin*, 1991), and extends from the ground and up to the exobase. The old version consisted of data from ground, rocket and satellite measurements from 1965 to 1983. The new model data also consists of mass density measurements from satellite accelerometers and orbital drag calculations. The model also includes solar UV occultation data, between 140 and 220 km altitude, $\pm 45°$ latitude, and a new component of "anomalous oxygen", that is O^+ and O_{hot}, at altitudes above 500 km. The temperature data from incoherent scatter radar measurements are also extended for the period 1981-1997. The radar data have directly influence on the model temperature, as these are the base for the MSIS models.

For the situations not covered by the empirical database, time intervals and locations without measurements and variable geophysical conditions, the composition and temperature are estimated from interpolation or extrapolation of the underlying data sets. At higher latitudes and for high geomagnetic activity, the database for the model is rater sparse. Since the model displays statistical averages, the local structure and fluctuations on shorter timescales of the atmosphere during a geomagnetic storm, are not captured.

The NRLMSISE-00 model can have daily 10.7 cm solar radio flux, and 3 hour Ap geomagnetic index as input parameters. For the lower latitude region and low geomagnetic activity ($Ap < 10$), the NRLMSISE-00 model appears to give an adequate representation of the lower thermospheric neutral atmosphere. This is certified by the comparison study of *Barth and Bailey* (2004), where the NO_x photochemical model with background parameters from NRLMSISE-00, gave a high correlation with the measured nitric oxide profile.

The MSIS models are based on a hydrostatic model (*Bates*, 1959). During periods of strong Joule heating, the atmosphere in the auroral regions will expand. This will bring up air that has a higher mixing ratio of molecules than of atoms, and is hence denser. The ion-neutral coupling, and the convection across the pole in the anti-sunward direction, will transport the molecule-rich air to mid-latitudes also. This will take place mainly around local midnight, but as the regions co-rotate with the Earth the disturbed regions

will spread to the morning sector as well. When the air in the auroral regions is lifted up, air from the lower latitudes will be brought in by the poleward return flow of the neutral winds (*Burns et al.*, 2006). This air has a lower molecular mixing ratio than the air in the auroral oval. From the circulation described above, the air that is less dense (from the lower latitudes) will be situated beneath a layer of air that is more dense (from the auroral latitudes)(*Burns et al.*, 2006). This is displayed in Figure 2.8, at middle latitudes (around 30°) at pressures around z=-3 (about 135 km) at hours just after the storm (1800 UT) and at the end of the main phase of the storm (0000 UT). For these regions, where a layer of small N_2 mixing ratios lie under a layer of higher N_2 mixing ratios, the hydrostatic balance is not sustained. This feature is a strong deviation from the neutral atmosphere derived by *Bates* (1959). The results of *Burns et al.* (2006) are from a general circulation model, and it is likely that processes not included in the model would restore the atmosphere rapidly back to equilibrium again. Gravity waves could be one of these processes. However, during a significant Joule heating event, the assumption of hydrostatic equilibrium in the lower thermosphere will not be valid, and the MSIS empirical models may not give correct answers.

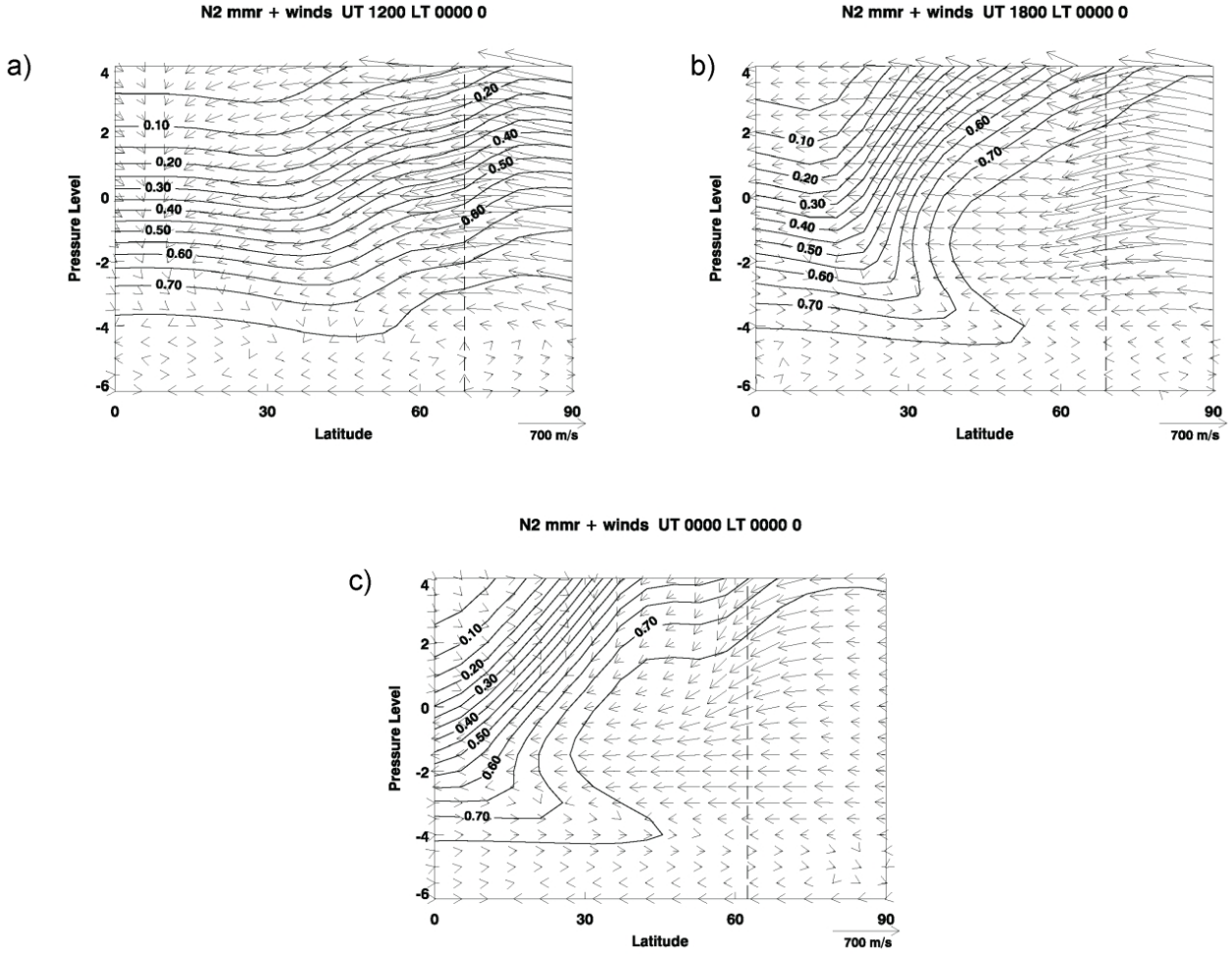

Figure 2.8: Modeled changes in N_2 mass mixing ratio (dimensionless) in the vertical direction (∼100 km altitude at z=-6, ∼135 km at z=-3, and ∼450 km at z=4). a) 1200 UT, before storm. b) 1800 UT, right after storm onset. c) 0000 UT, at the end of the main phase of the storm. The arrows are the neutral winds in the meridional direction. All three plots are for 0000 SLT. The dashed line indicates the auroral oval. z is the pressure surface, and the z=0 surface corresponds to a height of ∼280km. The figure is from *Burns et al.* (2006)

Chapter 3

Instruments and techniques

This chapter describes in short the satellite instrumentation of the SNOE project, in particular the ultraviolet instrument for nitric oxide measurements. The techniques used for deriving the particular parameters are described. The photochemical model used in Papers II and III for calculation of thermospheric nitric oxide, is also described. The Polar spacecraft and the two global auroral imaging experiments, UVI and PIXIE, are presented in the last sections of the chapter.

3.1 SNOE

The Student Nitric Oxide Explorer (SNOE) was a student satellite project at the University of Colorado (*Solomon et al.*, 1996). The scientific objectives of SNOE were to find how the NO density variations related to changes in the solar soft X-ray radiation, and to find the amount of NO production by auroral precipitation in the polar regions. It was in a circular Sun-synchronous orbit at ∼550 km altitude, with a 97.5° inclination, and ascending node at ∼1030 SLT. A sketch of the orbit is shown in Figure 3.1. The orbital period was 96 minutes, and it had a spin period of 12 seconds. The satellite was relatively small, weighing only 125 kg, and carried four instruments. The first of the instruments was an ultraviolet spectrometer (UVS) for measurements of nitric oxide densities between 96-150 km altitude, by observing the (1,0) and (0,1)

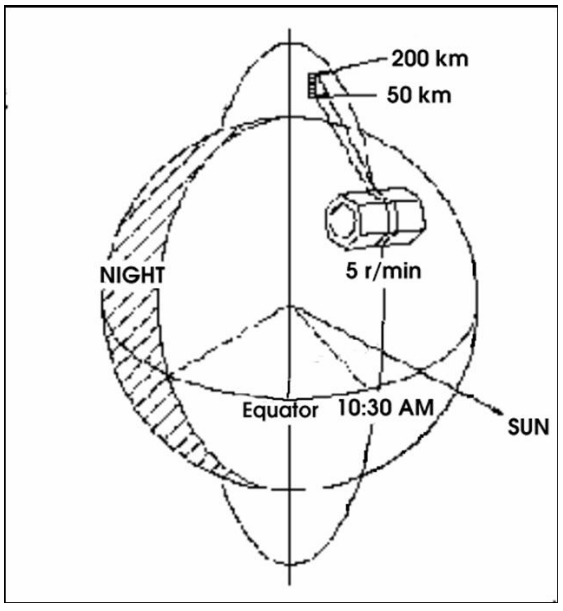

Figure 3.1: Orbit of the SNOE satellite

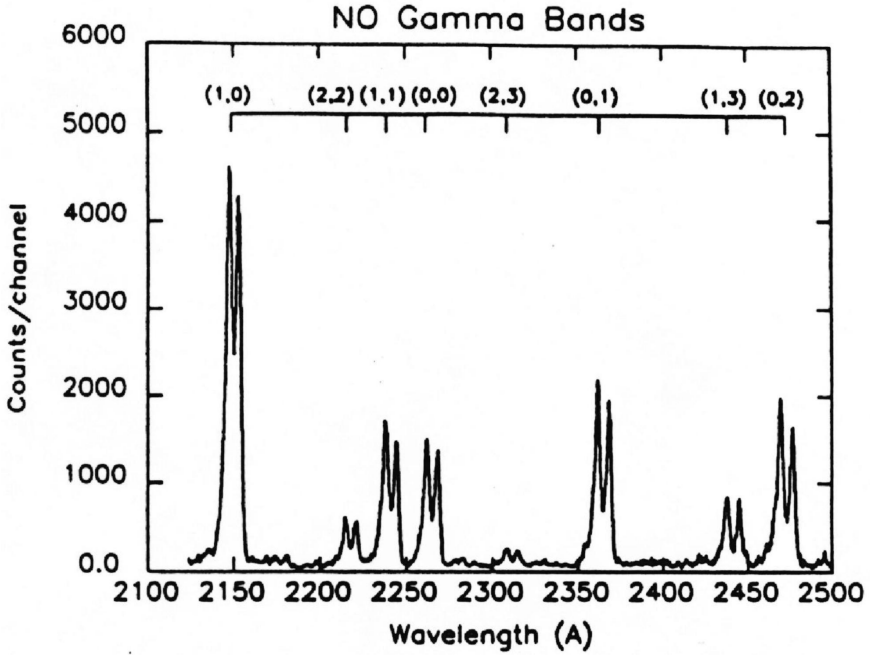

Figure 3.2: Nitric oxide gamma band emissions. The spectrum is of the Earth's dayglow, from 210 nm to 250 nm. It is made from the sum of spectral scans between 100 and 110 km altitude by a rocket experiment in March 1989 (*Eparvier and Barth*, 1992).

gamma band emissions from fluorescence of NO by solar radiation. An emission spectrum of the NO gamma bands is shown in Figure 3.2. The most intense emission is the (1,0) band. The (0,1) band is the second most intense gamma band emission, $\sim \frac{1}{2}$ of the (1,0) band intensity. Within the 96-150 km altitude region the contamination from other airglow emissions and from polar mesospheric clouds are minimal. Above 130 km there might still be some contribution in the data from the N_2 Vegard-Kaplan (0,3) band though (*Eparvier and Barth*, 1992). The nitric oxide gamma band system arises from electronic transitions between the ground $X^2\Pi$ state and the excited $A^2\Sigma^+$ state of NO. The individual bands of the system are the results of vibrational transitions, and each band is again composed of many, many lines arising from rotational transitions. The UVS consisted of an Ebert-Fastie spectrometer, an off-axis telescope, and two phototube detectors, one for each of the gamma bands. The bandpasses of both channels were 3.8 nm. The optical axis of the UVS was perpendicular to the spin axis of the satellite. The imaging of the Earth limb had a 3.2 km (altitude) by 33 km (longitude) field-of-view, at a distance of $\sim$2500 km. As SNOE moved $\sim$0.75° along it's orbit each spin, and the UVS data were averaged over six consecutive spins, the latitudinal resolution was about 5°. Due to the spinning motion of SNOE, the UVS also measured the Rayleigh scattering of sunlight from the atmosphere. Below 70 km altitude the observations were completely dominated by this Rayleigh scattered radiation. These measurements were used for altitude determination of the SNOE UV measurements (*Merkel et al.*, 2001).

The second instrument on board SNOE was the auroral photometer (AP), which measured the nighttime ultraviolet auroral emissions in the Lyman-Birge-Hopfield bands, the O_I doublet at 135.6 nm, and the O_I triplet at 130.4 nm. On the dayside of the orbit, the instrument was used for observation of the far ultraviolet dayglow. This instrument was designed for determining the auroral electron energy deposition in the upper atmosphere. The viewing angle of the instrument was in the nadir direction.

Solomon et al. (1999) used the measurements from the auroral photometer to obtain an indication of the auroral activity, from the position of the measured equatorward boundary of the auroral oval on the nightside. The technique was developed for use with Defense Meteorological Satellite Program (DMSP) energetic electron data, and the "midnight boundary index" was shown to be a good overall indicator of auroral activity and total energy flux (*Gussenhoven et al.*, 1981, 1983; *Hardy et al.*, 1985). The measured equatorward boundary of the auroral precipitation region was mapped to the equivalent position at midnight magnetic local time (MLT). For the SNOE auroral data, with MLT measurements only a couple of hours from midnight, the adjustments were minor. The SNOE midnight auroral boundary correlated well with the midnight boundary index from the DMSP dataset, as well as other magnetic-based indices. The daily averaged nitric oxide density derived from the UV spectrometer measurements of the NO dayglow, was averaged over the altitude region from 100 to 160 km, and over auroral latitudes. The NO density was compared with the daily averaged midnight auroral boundary index, for the first 81 days of the SNOE measurements. The strongest correlation (r=0.8) was found when the NO density was compared to the previous day auroral activity level.

The third instrument was a solar X-ray photometer (SXP), for measurements of the solar irradiance in the wavelength region 2-20 nm. Three photodiodes coated with thin metallic films provided the X-ray measurements, where different types of metals gave different passbands for the photodiodes. The viewing angle of the instrument was toward the sun, perpendicular to the orbital plane of the satellite. The irradiance measured by SXP had a clear 27-day periodicity, and was strongly correlated with the solar F10.7 index (*Bailey et al.*, 2000).

The fourth instrument was a GPS receiver for orbit determination. Both ground based laboratory and in-flight calibrations were performed for sensitivity determination of the instruments (*Barth et al.*, 2003; *Bailey et al.*, 2000).

The nitric oxide density data from the SNOE experiment used in this thesis were based on observations from the (0,1) 237 nm channel of the UV spectrometer. This emission line is not as strong as the (1,0) 215 nm channel, but unlike the (1,0) band it is not in resonance with the emission process for the band. That is the (0,1) band is optically thin and do not experience any self-absorption on its way out of the atmosphere. The combination of measurements from the two emission bands, can be used for verification of the sensitivity of the instrument by a self-absorption technique (*Eparvier and Barth*, 1992). The (0,1) optically thin column emissions are related to the column nitric oxide density through the emission rate factor, g, for the emission. The g-factor gives the number of photons

scattered per second per molecular unit for the spectral band $\nu'\nu''$,

$$g_{\nu'\nu''} = \pi F \frac{\pi e^2}{mc^2} \lambda^2 f_{\nu'\nu''} \omega_{\nu'\nu''} \tag{3.1}$$

Where πF is the solar irradiance, $(\pi e^2)/(mc^2)$ is a constant, λ is the wavelength of the emission line, $f_{\nu'\nu''}$ is the band's oscillator strength, and $\omega_{\nu'\nu''}$ is the branching ratio of the band. The latter two are determined in laboratory experiments. The g-factor is in simple words a measure for the possibility of absorption of solar radiation at a wavelength, and the subsequent possibility for fluorescent emission. The g-factor depends mainly on the heliocentric distance, on Doppler effects on the emission lines, on the rotational temperature of the molecule, on the solar activity, and on the optical depth of the emission line. The volume density of NO from the SNOE measurements was derived through an onionskin inversion algorithm (*McCoy*, 1983). The atmosphere was divided vertically in shells, 3.3 km thick, where the volume emission rate was assumed to be uniform within each shell.

In Paper I the SNOE Version 1 data were used, which had a g-factor for the (0,1) gamma band of 2.25×10^{-6} photons/sec-molecule (*Barth et al.*, 2003). The heliocentric distance of the Earth was accounted for, and the solar flux at 226 nm was from the Spacelab 2 Shuttle Solar Ultraviolet Spectral Irradiance Monitor (*VanHoosier et al.*, 1988). The solar flux (0.1 nm resolution) was used together with rocket measurements of the NO gamma band emissions to calculate g-factors for both the (0,1) and (1,0) emission bands (*Eparvier and Barth*, 1992). The oscillator strengths were from *Farmer et al.* (1972) and the branching ratios for the emission bands were from *Piper and Cowles* (1986).

In Paper II and Paper III, the Version 2 SNOE data were used. The (0,1) band g-factor was now set to the average value of 2.63×10^{-6} photons/sec-molecule (*Barth and Bailey*, 2004). Figure 3.3 gives the g-factor value (Version 2) for the (0,1) gamma band. The g-factor varies clearly with the heliocentric distance of the Earth, and with the solar activity. The solar flux at 226 nm was now from measurements by the Solar-Stellar Irradiance Comparison Experiment (SOLSTICE) on UARS (*Rottman et al.*, 1993). The g-factors were adopted from the work of *Stevens* (1995), where they were calculated from a solar spectrum measured from a balloon flight (0.01 nm resolution). The spectrum was normalized to the SOLSTICE measurements (1 nm resolution) for 25 February 1992. The oscillator strength and the branching ratio for the emission band, were the same as for the Version 1 data. Hence, the only difference was the solar spectrum measurements. Due to strong absorption lines in the solar spectrum, it is important to have high-resolution spectra. In addition the *Stevens* (1995) calculations involved a more extensive nitric oxide rotational structure. The g-factor used in the Version 1 SNOE data was 14% less than the value used in the Version 2 dataset. The new solar flux measurements account for 10%, and the more complete rotational structure accounts for the remaining 4% of the difference (*Barth and Bailey*, 2004).

The lifetime of a ground state NO molecule is one day or more, whereas the time between collisions of the NO molecules and the surrounding atmospheric species is $\sim$1/10 seconds. The lifetime of the excited NO molecule to radiative decay is just a couple of hundred nanoseconds for the gamma bands (*Langhoff et al.*, 1988). From this, it is a

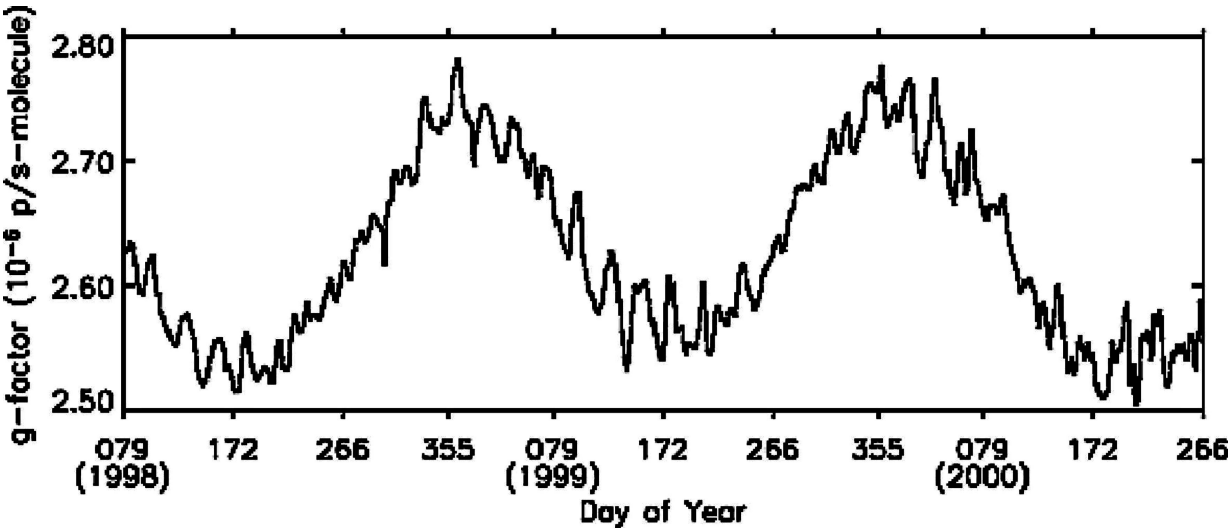

Figure 3.3: The g-factor value for the (0,1) nitric oxide gamma band for the period of SNOE observations, Figure 2 of *Barth and Bailey* (2004). The variations are due to changing heliocentric distance and solar activity.

decent assumption that the ground state NO gas is in thermal equilibrium with the ambient atmosphere.

3.2 NO_x photochemical model

Bailey et al. (2002) made an updated version of a photochemical model for nitric oxides in the lower thermosphere (*Cleary*, 1986; *Barth*, 1992). This version was designed for the analysis of nitric oxide data from the SNOE satellite, and one of the input parameters is the solar soft X-rays also measured by SNOE. The model is time dependent, it calculates the energetic electron flux including vertical diffusion, and it involves the neutral and ion chemistry of NO, $N(^4S)$, $N(^2D)$, N_2^+, O_2^+, O^+, and NO^+. The model does not include neutral wind. However, it calculates the vertical eddy and molecular diffusion for NO and $N(^4S)$.

The calculation of energetic electron impact on the ionization and dissociation is done by use of the *glow* model (*Solomon et al.*, 1988; *Solomon and Abreu*, 1989). This electron transport algorithm is based on the two-stream code of *Banks and Nagy* (1970), and is extended to higher electron energies for auroral computation. The code calculates the upward and downward hemispherical fluxes along magnetic field lines as a function of electron energy. Gravity, parallel electric fields, and magnetic field convergence are neglected in the calculations. The discrete energy loss from inelastic collisions with the main neutral constituents (O, N_2, and O_2), causing excitation and ionization, and thermal energetization of the ambient ionospheric electrons are considered. The code does not consider pitch angle variations, but assumes a constant pitch angle of 60° of the incoming electrons. Appendix

A in *Solomon et al.* (1988) gives the electron impact cross sections and backscatter ratios. The two-stream equations of the electron transport are (*Bailey et al.*, 2002):

$$\mu\frac{d\phi^+}{dz} = -T_2\phi^+ + T_1\phi^- + Q^+ + \frac{q}{2} \tag{3.2}$$

$$-\mu\frac{d\phi^-}{dz} = -T_2\phi^- + T_1\phi^+ + Q^- + \frac{q}{2} \tag{3.3}$$

Here ϕ^+ and ϕ^- are the upward and downward flux of electrons ($cm^{-2}s^{-1}$ as a function of electron energy and altitude), μ is the cosine of the pitch angle, z is the distance along the field line, q is the new production of photoelectrons from solar radiation, and Q is the cascade of electrons when higher energy electrons collide inelastic with the neutral gas. T_2 displays the electrons that are lost in inelastic collisions, and those who are scattered backwards after elastic collisions with the main neutral constituents. T_1 represents the electrons that are scattered backwards by electrons with initial path in the opposite direction, colliding elastically with the neutral gas. The boundary conditions of the electron transport equations are:
- At the top of the atmosphere: if aurora, the primary spectrum of energetic electrons, and if non-aurora, the downward flux is set to zero.
- The lower boundary: the downward flux and the upward flux are both set to zero.

The inputs to the photochemical model for solar irradiance are extreme ultraviolet (EUV) and solar soft X-rays. The EUV irradiance is from the model of *Hinteregger et al.* (1981), which has the 10.7 cm solar radio flux as input parameter. The solar soft X-rays are partly from SNOE measurements (2-20 nm), and partly calculated by the *Hinteregger et al.* (1981) model (20-103 nm). The model atmosphere for neutral species and temperatures is from the NRLMSISE-00 model (*Picone et al.*, 2002), which use the 10.7 cm solar radio flux and the Ap geomagnetic index as input parameters. The initial ionospheric electron and ion densities and temperatures are from the International Reference Ionosphere (IRI) (*Belitza*, 1986). The model calculations of photoelectron spectra using SNOE solar irradiance data, were found to correspond with measured photoelectron fluxes from the Atmosphere Explorer, AE-E, photoelectron spectrometer (*Solomon et al.*, 2001).

When the energetic electron spectrum is found at each altitude, the ionization, dissociation, and excitation rates by electron impact are calculated over all electron energies:

$$\int_0^\infty \phi(E,z)\sigma(E)n_s(z)dE \tag{3.4}$$

Where ϕ is still the photoelectron flux, σ is the cross section for the process at hand, and n_s is the number density of the atmospheric species undergoing the process. The number density is calculated by use of this simplified equation:

$$\frac{\delta n_s}{\delta t} = P_s - L_s n_s - \frac{\delta \phi_s}{\delta z} \tag{3.5}$$

Where P_s is the production rate of species s ($\mathrm{cm}^{-3}\ \mathrm{s}^{-1}$), and L_s is the loss rate of species s (s^{-1}). Calculation of the vertical flux of the NO or N(^{4}S), ϕ_s, includes molecular and

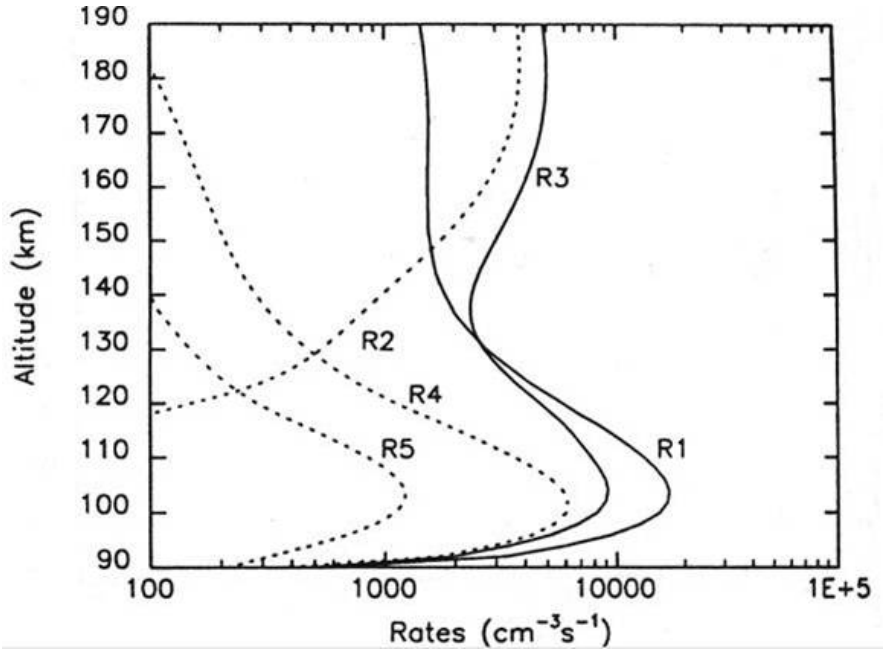

Figure 3.4: Reaction rates for the five most important nitric oxide reactions of the photochemical NO_x model, assuming an auroral electron flux of 1.5 ergs/sec cm^2 (Figure 8 in *Barth* (1995)). R1 is the production rate of NO from N(^{2}D)+O_2, and R2 is the production rate from N(^{4}S)+O_2. The loss rates R3, R4, and R5 are for the reaction of NO with N(^{4}S), with O_2^+, and photodissociation, respectively.

eddy diffusion and temperature gradients. The boundary conditions for NO and N(^{4}S) are no upward flux at the top of atmosphere (200 km), and for the bottom of the atmosphere (70 km) NO is assumed to be at a minimum, and N(^{4}S) is assumed to be in photochemical equilibrium. The model starts out with all of the minor species having zero values, and the major species coming from the NRLMSISE-00 model. Ionization and dissociation rates are from the *glow* model, and the calculations of the minor species are repeated until convergence.

The chemical reactions used in the NO_x model are given in *Barth* (1992) and in *Bailey et al.* (2002). The most important reaction rates for the NO chemistry are shown in Figure 3.4, as a function of altitude.

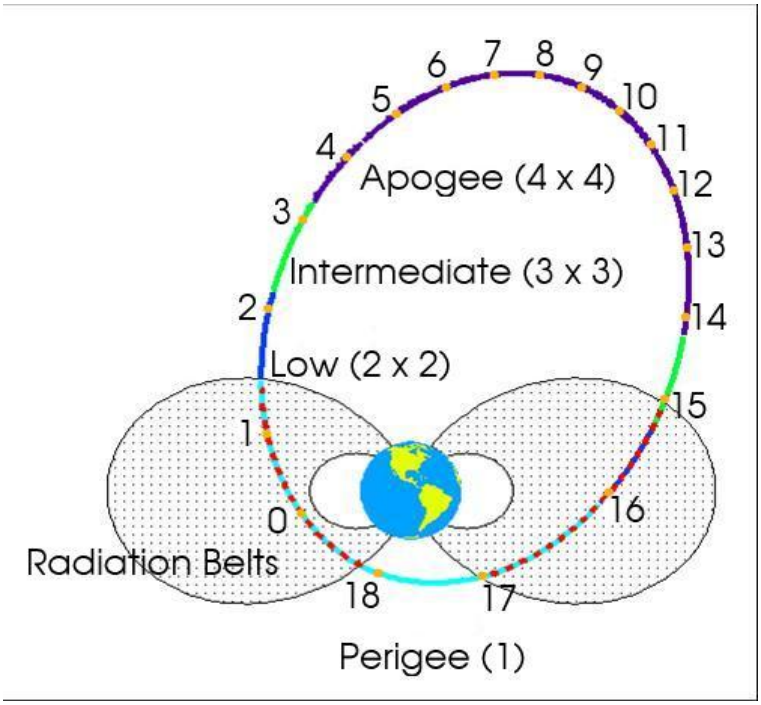

Figure 3.5: Orbit of the Polar spacecraft (1998) with 1 hour time steps, and the pinhole configuration of the PIXIE instrument (at apogee 4x4 pinholes).

3.3 Polar

The Polar spacecraft was a part of the Global Geospace Science program (*Acuña et al.*, 1995) and of the International Solar Terrestrial Physics (ISTP) program. It was launched 24 February 1996 in a highly elliptical orbit, with apogee at 9 earth radii and perigee at 1.8 earth radii (see Figure 3.5). The period of the orbit was ∼19 hours, and the inclination was 86°. Initially the apogee of the orbit was above the North Pole, but gradually it moved at ∼16° per year toward the equator. The mission objective for the Polar spacecraft was to obtain data from the polar regions at both high and low altitude. It had twelve scientific instruments, where three of them were for imaging of the aurora in different wavelengths. The remaining nine instruments made in-situ measurements of fluxes of charged particles, magnetic and electric fields, and electromagnetic waves (*Russel*, 1995). For the studies presented here, observations from the imaging instruments UVI and PIXIE have been used.

3.3.1 UVI

The Ultraviolet Imager (UVI) on board Polar, observes the aurora in the far ultraviolet (FUV) part of the spectrum for both sunlit and dark regions (*Torr et al.*, 1995). The bandpass of the instrument is 125.0-200.0 nm, where the principal emission lines are from Lyman-Birge-Hopfield (LBH) emissions from molecular nitrogen, and also some atomic nitrogen lines. The mission objective of the UVI instrument was to obtain information of

the solar-terrestrial coupling. By help of comprehensive models one can infer the energy flux and average energy of the precipitating electrons causing the UV emissions. One can also determine ionospheric conductances, and from them the electric potentials and convective patterns. UVI has also been used for studies of the morphology of the auroral emissions. Conjugate studies with magnetospheric measurements have been made, where the auroral patterns were traced back to their source regions in the magnetosphere.

In Paper III the UVI observations were used for deriving the energy flux and average energy of the precipitating electrons, in the energy range 0.2-25 keV. The technique for doing this is based on the different degrees of absorption of the short wavelength band of the LBH emissions (LBHs 140-160 nm), and of the long wavelength band (LBHl 160-180 nm) (*Germany et al.*, 1998a,b, 1997). The LBHl emissions experience nearly no absorption, and can be used to determine the flux of the incoming electrons. The LBHs emissions, however, experience strong absorption by the O_2 Shumann-Runge continuum. The higher energy precipitating electrons will deposit most of their energy lower down in the atmosphere, and the resulting emissions will thus be more absorbed on their way out. The ratio between the strongly absorbed band and the unabated one, can therefore be used for diagnostic of the average energy of the precipitating electrons. In the analysis, the LBH emissions are thought to be due solely to electron impact excitation. The contribution of the proton precipitation to the emissions are discussed in *Galand and Lummerzheim* (2004). They found that in some local times, especially the equatorward edge of the afternoon oval, the proton precipitation could contribute noticeable to the UVI response. In regions where the electron precipitation had a distribution $>$4 keV, the presence of proton aurora yields an underestimation of the electron mean energy. This is due to keV protons giving a response in the UVI measurements that is similar to the low energy electrons. The method for retrieving the electron energy flux from the UVI measurements, is to little extent affected by the proton aurora (*Galand and Lummerzheim*, 2004). Since the UVI measurements were used for deriving the spectra for the lower energy electrons ($<$4 keV), and PIXIE observations covered the higher energy part, the errors due to any proton precipitation are assumed to be negligible.

The UVI measurements have $\sim$2 minutes time-resolution, and the spatial resolution when Polar was at apogee was $\sim$360 km due to the wobbling of the pointable pedestal on the Polar spacecraft.

3.3.2 PIXIE

The Polar Ionospheric X-ray Imaging Experiment (PIXIE) on board the Polar spacecraft, was a multi-pinhole camera for imaging of X-ray bremsstrahlung. When electrons precipitate down in the atmosphere, they are slowed down in the coulomb field of the atmospheric molecules and atoms, and in this process X-rays are emitted.

PIXIE observed X-rays in the energy range $\sim$2-22 keV. The lower part ($\sim$2-9) of this energy range was observed by the front chamber of the PIXIE instrument, and the upper part by the rear chamber (*Imhof et al.*, 1995). The pinhole plates were designed so that the size of the pinholes could be adjusted for the different stages of the orbit, like a telescopic

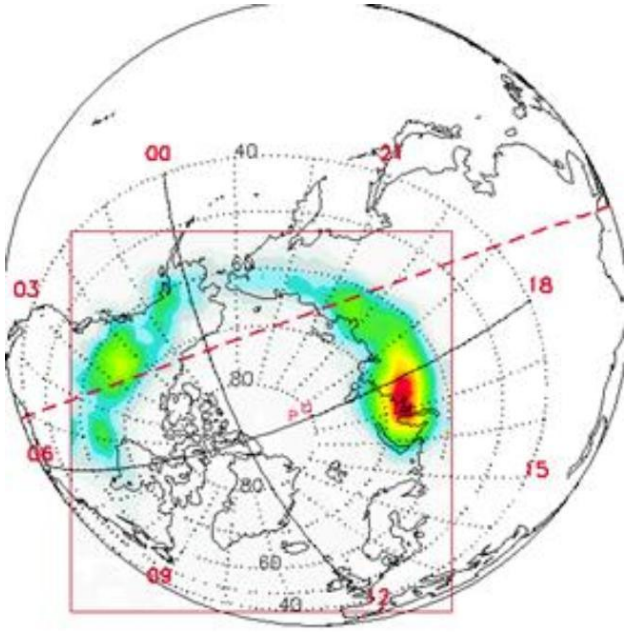

Figure 3.6: PIXIE bremsstrahlung measurement from the front chamber, 11:40-11:45 UT, 2 May 1998.

lens. The spatial resolution of the instrument was about 700 km for apogee.

The fraction of X-ray photons produced by the highly energetic electrons is quite small (*Berger and Seltzer*, 1972). In order to achieve good enough statistics for the PIXIE data, the accumulation time for apogee passes was in the studies described here, ∼5 minutes for the front chamber, and ∼10 minutes for the rear chamber. The front chamber had to be duty cycled due to an intermittent high voltage supply problem. In 1998 this part of the camera was typically on for ∼5 minutes, and off for ∼5 minutes. The rear chamber ran continuously until October 1998. An example of an image obtained from PIXIE's front chamber is shown in Figure 3.6. The entire auroral oval is captured within PIXIE's field of view.

There are models relating the X-ray bremsstrahlung production and the energetic electron precipitation, and for the PIXIE observations a look-up table for the incoming electron energy spectra and the produced X-ray spectra is used. This look-up table is based on a coupled electron/photon transport code, initially a model for neutral particle transport (*Lorence*, 1992). This method provides rather good agreement between measured electron energy fluxes, and that derived from PIXIE X-ray observations (*Østgaard et al.*, 1999; *Anderson et al.*, 1998).

The advantage of using PIXIE X-ray bremsstrahlung measurements, is that one obtains information of the higher energy electrons (∼4-100 keV) on a contemporary global scale. When investigating the auroral production of a chemical species like nitric oxide, the PIXIE observations are a very valuable tool. The data processing for the PIXIE observations is

described in *Østgaard et al.* (1999). During the image processing the raw energy and position data are binned in a 300×300 matrix for each of the six energy bands. Then the procedure corrects for the energy efficiency, the background is subtracted, and small scale non-linear effects are removed. Finally the corrected sub-images from the different pinholes are superimposed, smoothed, and projected down on the Earth at 100 km altitude. The method for deriving electron energy spectra from the PIXIE X-ray measurements is described in *Østgaard et al.* (2000). As mentioned above, a look-up table is used for relating the measured X-ray spectra to the electron precipitation. A Chi-square test is performed, and of the electron energy spectra that pass the test, the one that gives the smallest electron energy flux is used. Thus giving a lower limit of the electron energy flux deposited in the ionosphere based on the bremsstrahlung measurements. *Østgaard et al.* (2001) describes the technique for deriving electron energy spectra from the combined UVI and PIXIE measurements. The UVI measurements contribute to the lower energy part of the derived electron spectra (0.2-25 keV), and PIXIE to the upper energy part (4-100 keV). The final energy ranges for the electron spectra, are determined from what produces 90% of the observed UV emissions and X-rays. That means that the energy limits for the calculated electron spectrum vary with the derived mean electron energy.

The methods for analyzing the PIXIE data have been somewhat different for the three papers. The data analysis will therefore be presented in the next chapter on the Summary of papers.

3.4 Magnetometer database: SuperMAG

Magnetometer chain:	**# st.:**	**web:**
Intermagnet	99	www.intermagnet.org
Greenland	22	web.dmi.dk
Carisma	13	bluebird.phys.ualberta.ca/carisma/
Image	27	www.ava.fmi.fi/image/
SAMBA	11	samba.atmos.ucla.edu
SAMNET	18	www.dcs.lancs.ac.uk/iono/samnet/
MEASURE	10	measure.igpp.ucla.edu/
MACCS	13	space.augsburg.edu/space
210 Chain	37	stdb2.stelab.nagoya-u.ac.jp/mm210/
AARI	13	www.aari.nw.ru/clgmi/geophys/mag_main.htm
USGS	14	geomag.usgs.gov
GIMA	8	magnet.gi.alaska.edu

Table 3.1: The magnetometer stations involved in the SuperMAG collaboration, the number of stations, and the webpages for each of the chains.

The Global Magnetometer Network, SuperMAG, is a data set provided by more than

200 ground magnetometer stations (*Gjerloev et al.*, 2004). This gives nearly global and continuous measurements of the ground level magnetic field perturbations. The database is organized in the same data format, with a common coordinate system and time resolution, and the same method for baseline removal. The ground magnetic components are divided in geomagnetic north (N), east (E), and vertically down (Z) components. The scientific objective of the SuperMAG database is to study the coupling between the ionosphere and the magnetosphere on a global scale. The main focus is the horizontal ionospheric current systems and their connection to the magnetosphere through the field aligned currents. The magnetometer chains contributing to the SuperMAG dataset, are listed in Table 3.1. Figure 3.7 shows the distribution of the geomagnetic stations in the northern hemisphere (north of 40°N). In Paper III these stations were used for a parametrization of the electron energy flux.

The auroral electrons deposit their energy in the atmosphere through ionization, dissociation, particle heating and excitation. The ionization processes give an increased electron density in the ionosphere, and thereby an increased conductance. The Pedersen conductance, for currents along the electric field perpendicular to the magnetic field, is related to the Joule heating. The Hall conductance is for currents perpendicular to both the parallel electric field and the magnetic field. These currents are called Hall currents. In the ionosphere these flow mainly in the zonal direction, that is east or west. On the ground, the Hall currents induce perturbations in the north/south component of the geomagnetic field. The westward flowing current gives a decrease of the north component of the magnetic field, and eastward flowing gives an increase. The maximum positive deviation of the north component of the geomagnetic field in the entire auroral zone, is used for the geomagnetic index, AU. The maximum negative deviation of the north component in the auroral regions, is the AL index. The sum of the absolute values of these two, is the AE index.

The auroral electron energy deposition is related to the AE index from the increase of electron density, giving an increased conductivity, and hence stronger Hall currents. The eastward currents flow in the evening sector, and the westward currents flow in the morning and midnight sectors. The strongest parts of the currents on the night side, are called the eastward and westward electrojets. The AU index is found to be more modulated by the electric field and the dayside solar Hall conductance, than by the electron precipitation. While the Hall conductance, governed by auroral electrons, is more important for the AL index (*Ahn et al.*, 1999; *Gjerloev and Hoffmann*, 2001). Two schematic models for the ionospheric substorm, with electric field vectors and current systems, are shown in Figure 3.8. The dominance of conductance in the premidnight sector, is related to the typical energetic electron precipitation (>10 keV) in that region. In the postmidnight and dawn sectors, the electrojet system is driven by a mix of the equatorward electric field and the Hall conductance.

In Paper III the perturbations in the negative north component were used for parametrization of the auroral electron flux. Using geomagnetic indices for estimation of the particle precipitation, has been done in several previous studies (e.g. *Akasofu*, 1981; *Ahn et al.*, 1983; *Lu et al.*, 1998; *Østgaard et al.*, 2002). These studies have used the global indices,

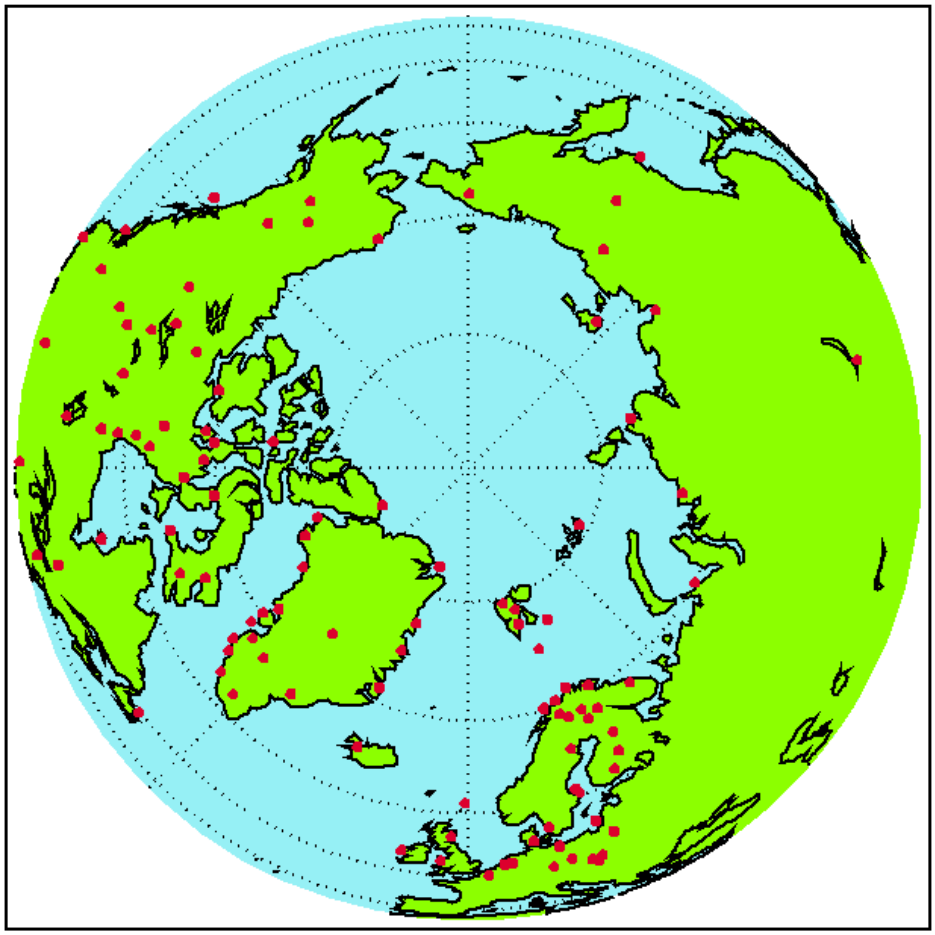

Figure 3.7: The distribution of geomagnetic stations (red dots) in the northern hemisphere included in the SuperMAG database.

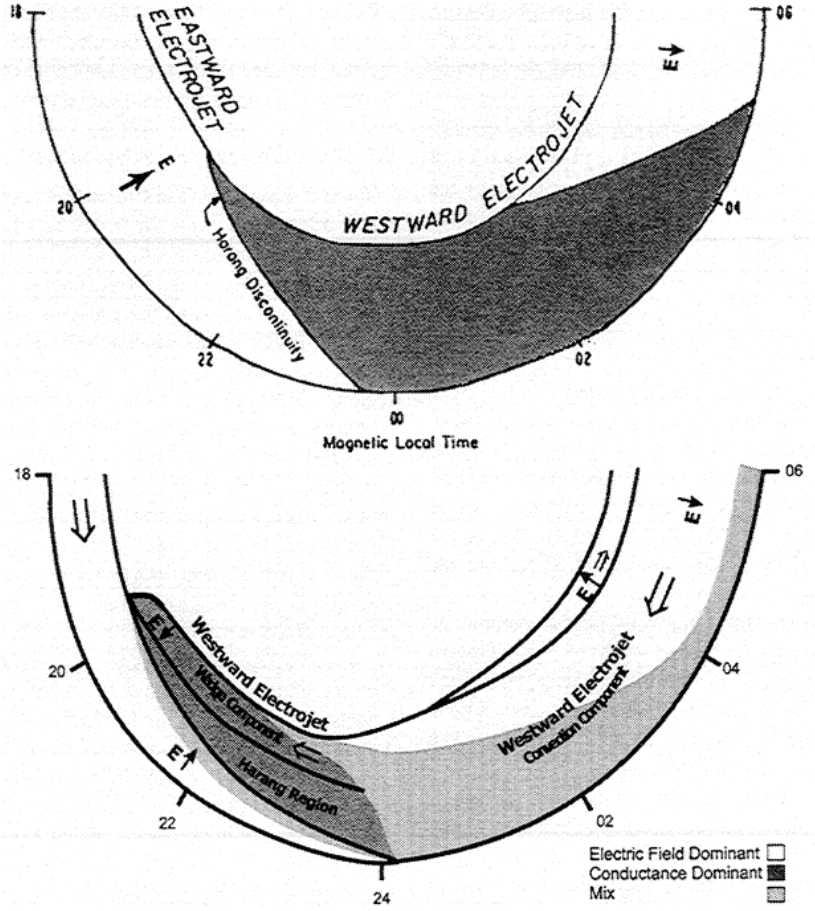

Figure 3.8: Two schematic models of the electrojet system in the ionosphere. The upper one is from *Kamide and Kokubun* (1996), and the lower one from *Gjerloev and Hoffmann* (2001); *Gjerloev and Hoffman* (2000). The conductance dominated regions are in dark gray. In these regions the Hall conductance exceeds the electric field by more than 20%. The white regions are for electric field dominance, more than 20% of the conductance. The light gray is for the mixed regions.

mainly for deriving the total auroral energy deposition, U_A. What is new for the study presented here, is to use the local geomagnetic perturbations in 24° geographical longitude sectors. A geographical coordinate system is chosen for employing the parametrization to the neutral chemistry model.

The SuperMAG network in the northern hemisphere consists of many enough stations to divide them into fifteen longitude sectors. In some of the regions, mainly the Siberia, there are only one or two stations per 24° longitude sector. For these regions, the risk is to underestimate the auroral energy flux. For the regions with more than one station, the maximum negative deviation in the north component ($\Delta N<0$) for all the stations within the sector is used. The perturbations (nT) are compared to the electron energy flux (mW m^{-2}) derived from UVI and PIXIE measurements. The electron flux is also divided in 24° longitude sectors, and averaged over the latitude region between 50°N-70°N. Since the comparisons are done for the same local time sectors, and not by using a global geomagnetic index, one has information on which current system that most likely contributes to the magnetometer data. On the dayside, as mentioned above, the magnetic perturbations are dominated by the electric field, and not necessarily connected to the electron precipitation. For the events used in the comparisons for Paper III, the local $\Delta N<0$ values are typically quite low on the dayside. The dayside magnetometer data are included in the comparisons, assuming they are a minor factor for the uncertainty of the parametrization.

Chapter 4

Summary of papers

In this chapter a short summary is given for each of the three papers of the thesis. The governing idea linking these papers together, is the understanding of the nitric oxide variations in the lower thermosphere in relation to auroral electron precipitation. The nitric oxide density was derived from SNOE airglow measurements, and from calculations by a photochemical model for nitric oxides. The auroral electron precipitation was derived from auroral bremsstrahlung and ultraviolet emissions observed by PIXIE and UVI, on board Polar. In Paper III the auroral electron energy flux was also estimated from ground magnetic measurements, from the SuperMAG database.

4.1 Paper I: Energetic electron precipitation and the NO abundance in the upper atmosphere: A direct comparison during a geomagnetic storm

This study presented the first direct comparisons between time-integrated energetic electron precipitation, and the observed nitric oxide density in the lower thermosphere for a specific case. Previous studies had compared the daily averages of these two parameters. The electron precipitation used, was derived from X-ray bremsstrahlung measurements from the Polar Ionospheric X-ray Imaging Experiment (PIXIE). The nitric oxide volume densities were the Version 1 measurements from the Student Nitric Oxide Explorer (SNOE). The comparisons were done for a geomagnetic storm event on 2 May 1998, where the geomagnetic conditions were rather quiet two days before the storm onset. The motivation for doing this study, was much based on prior work done by *Barth et al.* (1999) and *Petrinec et al.* (2003), discussed in Chapter 2.

Since PIXIE observed the full auroral oval of the northern hemisphere for almost ten continuous hours a day in 1998, it would be possible to compare the auroral bremsstrahlung with the observed dayside NO density in spite of the different timescales. The idea was to integrate over time the X-ray observations in geographical areas. As time goes on and the Earth rotates, new areas are exposed to auroral precipitation. And the "old" areas, of

Images from PIXIE:

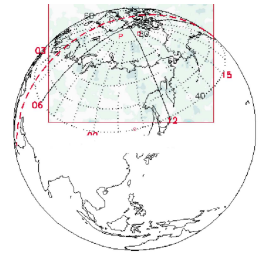

02:20 - 02:25 UT

+

:

+

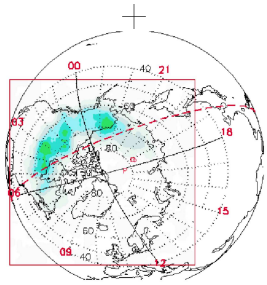

10:10 - 10:15 UT

+

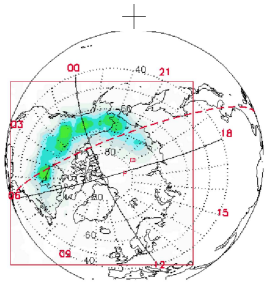

10:20 - 10:25 UT

Due to the long lifetime of NO, we have accumulated the electron precipitation (represented by the bremsstrahlung intensity) over several hours, before comparing with the NO-concentration.

Every 10. minute we generate global images of the X-ray intensity measured over 5 minutes. The intensity is assumed to stay constant within the 10 minute interval.

We are time-integrating the X-ray intensity in geographical boxes (4° longitude * 2° latitude), here from time of start 02:20 UT (well before start of substorm) to 10:25 UT.

$\longrightarrow$

Time-integrated X-ray bremsstrahlung (2-9 keV):

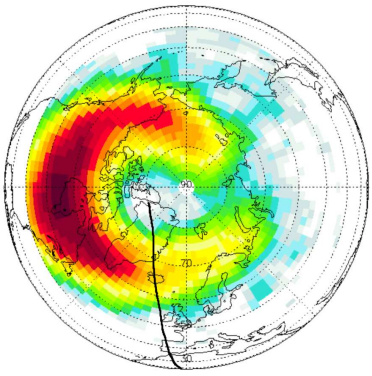

2. May 1998 02:20 - 10:25 UT

Black line: SNOE dayside orbit at ~10:30 SLT

Figure 4.1: An illustration of the procedure for adding PIXIE images (5 minute resolution for the front chamber, 10 minute time steps). The result is shown on the right, with the accumulated bremsstrahlung intensity (2-9 keV) in a geographical grid. Here the accumulation goes from 02:20 UT until 10:25 UT.

course, co-rotate with the Earth to the dayside. The total integrated X-ray intensity can then be compared with the observed NO density on the dayside of the SNOE orbit. The loss processes of NO are assumed to be governed by the NO abundance and the solar zenith angle. During geomagnetic storms, the production of NO from solar soft X-rays is negligible at higher latitudes, compared to the production due to auroral electron precipitation.

Figure 4.1 displays the method for obtaining the total auroral bremsstrahlung intensity for geographical areas throughout the night and morning. The X-ray images were partitioned in geographical boxes, 4° longitude and 2° latitude, from 40°N up to 80°N. The integration was done from the start time of PIXIE measurement, before the storm onset, and then until the time of each of the SNOE orbits used for comparisons. The original PIXIE X-ray images had an accumulation time of ∼5 minutes for the front chamber (2-9 keV X-ray energies) and ∼10 minutes for the back chamber (9-20 keV X-ray energies). The lower energy X-ray intensities were assumed to be constant over the 10 minute intervals. The time-integrated X-ray intensities were separated in 6 energy channels, and it was possible to fit the intensities with an exponential energy spectrum. For the calculations of the spectra the geographical box size was set to 5° latitude and 12° longitude. Due to the long intervals of time-integration, the measurement uncertainties for the PIXIE data for the six channels were quite low. By use of a look-up table based on a transport code of *Lorence* (1992), the electron energy spectrum corresponding to the time-integrated measured X-ray spectrum was found. The total electron energy deposition for a geographic area, throughout the night and morning hours, was thus found from these time-integrated X-ray measurements. The method for deriving the energy deposition was based on the work of *Rees* (1963) and the equations from chapter 3 of *Rees* (1989). The angular distribution of the precipitating electrons was assumed to be isotropic over the downward hemisphere. The mass density as a function of altitude was from the Mass Spectrometer and Incoherent Scatter Extended atmospheric model (MSISE-90). The energy deposition as a function of altitude and electron energy, was calculated with the total electron energy flux as input. The effective range of the electrons is given in (*Rees*, 1989), and is a function of the electron energy.

In Paper I the time-integrated X-ray intensities for the geographic regions, beneath each of the different SNOE orbits, were compared with the respective NO density measurements. These comparisons were done as a function of latitude for 110 km altitude. The comparisons showed tendencies of an equatorward drift of the NO density profile compared to the observed total bremsstrahlung intensity. The latitudinal resolution of the measurements were, however, not sufficient enough to prove this. Figure 4.2 shows the average horizontal neutral wind at 109 km altitude, 70°N, from quiet summer day radar measurements. From midnight until ∼08 SLT, the wind pattern had a clear southward component, which would in case result in an equatorward shift of the NO density profile.

The total electron energy deposition versus altitude, derived from the time-integrated X-ray measurements, was also compared to the NO density measured by SNOE. The altitude profiles (Paper I, Figure 5), were not expected to correlate directly. The NO density height profile is complicated by the different production and loss rates, and how they vary as a function of altitude (e.g. *Barth*, 1992; *Petrinec et al.*, 2003). The NO altitude

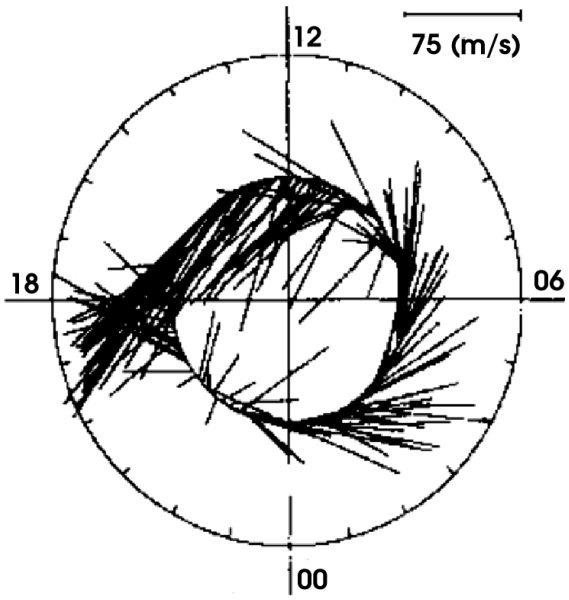

Figure 4.2: Horizontal neutral wind at 109 km altitude as a function of solar local time along the latitude of Tromsø. Average of EISCAT radar measurements for 7 geomagnetic quiet summer days. (Part of Figure 3 of *Brekke et al.* (1994).)

profile can also be affected by vertical winds as the atmosphere expands due to particle and Joule heating. The reaction rates involving NO are also more or less dependent on the atmospheric neutral temperature.

The altitude of the maximum electron energy deposition varied between 100-115 km, as did the altitude of maximum NO density. In general, when disregarding the amplitudes, the altitude profiles did not differ much. The NO density and the total electron energy deposition at 106 km altitude were compared as a function of latitude for each SNOE orbit. The linear relation between the measured NO density and the total electron energy deposition at 106 km altitude for the 2 May 1998 event, had a correlation of 0.9. The conclusion of Paper I was thus that the observed increase in NO on the dayside was clearly related to the total electron precipitation for the particular geographic region throughout the night and morning of 2 May 1998.

The NO density at 106 km altitude measured by SNOE, has also been compared with the total energy deposition (keV cm^{-3}) from PIXIE observations of four other events: 21 March, 14 and 26 June, and 16 July, 1998. The comparisons are shown in Figure 4.3. Also for these days there was a rather good correlation between the NO density and the accumulated energy deposited by auroral electrons in the areas of the SNOE observations. The slopes of the linear fits were somewhat different. At this stage, however, the main focus was the correlation between the NO variations and the electron energy deposition, not the absolute values. In Papers II and III the amount of NO produced from auroral electron precipitation was investigated by use of a photochemical model for nitric oxide.

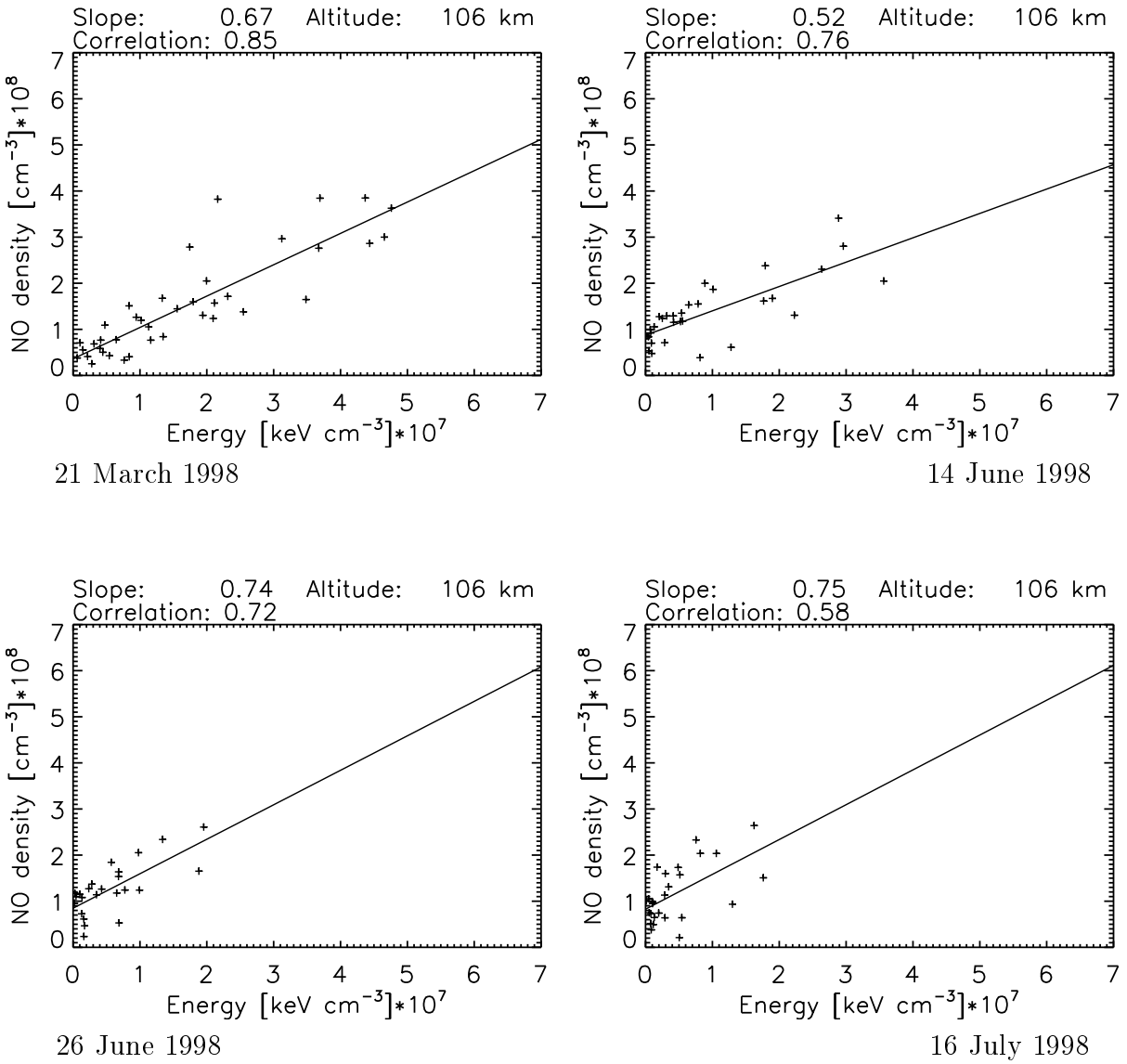

Figure 4.3: Nitric oxide density at 106 km altitude measured by SNOE, plotted against the total electron energy deposition derived from PIXIE measurements. The comparisons were for four days in 1998 where the geomagnetic activity level was rather low the preceding day. The slope and correlation of the linear fit between the two datasets are given for each plot.

4.2 Paper II: Comparisons of electron energy deposition derived from observations of lower thermospheric nitric oxide and from X-ray bremsstrahlung measurements.

The motivation for this study was to test the understanding of the physics and chemistry in the thermosphere, considering the energy transfer from solar processes into the Earth's upper atmosphere. The correlation between the variations of thermospheric nitric oxide at higher latitudes, with the variation in auroral electron energy input, was shown in Paper I. Paper II investigated the amplitude of the variation, based on the theory of nitric oxide (e.g. *Barth*, 1992).

A photochemical model for nitric oxides in the lower thermosphere, calculated the NO density with an adjustable auroral electron energy flux. The auroral electrons were assumed to have a maxwellian energy distribution with a characteristic energy of 4 keV. In Paper II the local time interval of auroral activity was set to 3 hours in the model, from 2100 to 2400 SLT. The solar soft X-rays measured by SNOE were input to the model. And the solar EUV radiation was modeled with the 10.7 cm radio flux as input (*Hinteregger et al.*, 1981). These parameters were used for calculating the production of NO from photoelectrons. The *glow* model of *Solomon et al.* (1988) calculated the electron transport, and the NRLMSISE-00 model provided the background atmosphere (*Picone et al.*, 2002). With this method one can obtain the auroral electron energy flux, for which the calculated nitric oxide density equals the NO density at 110 km altitude, as measured by SNOE. This electron flux was compared to the electron energy flux derived from PIXIE bremsstrahlung measurements. The concept of using the NO_x photochemical model to deduce the flux of precipitating energetic electrons, was first introduced in *Barth et al.* (2004). They compared the model calculations with the daily averaged SNOE NO data, for high latitudes at 110 km altitude. With two and a half years of SNOE data, the seasonal variability of the auroral electron precipitation was investigated.

The comparisons in Paper II were made for five geomagnetic storms in 1998, in the period where there were SNOE data and measurements from both chambers of the PIXIE instrument. The premises for the events were fairly quiet conditions on the day prior to the storm, and good coverage of PIXIE data. The events used in the study were 21 March, 2 May, 14 June, 26 June and 16 July. From the work related to Paper I, the correlation between the time-integrated electron energy deposition derived from PIXIE, and the NO density measured by SNOE for these days were quite good (see Figure 4.3, and Paper I). The variations of the observed NO density at higher latitudes were thus assumed to be directly related to the accumulated auroral electron energy deposition.

The principle for deriving the electron energy deposition from the PIXIE bremsstrahlung energy spectra, is described in Chapter 3. The electron energy flux was found by integrating the electrons within this energy range. The same was done for the spectra derived from the SNOE NO measurements, so that the energy fluxes were comparable. The PIXIE

derived electron energy flux was integrated over time, so the unit for the total auroral energy deposition was keV/cm^2. The energy deposition modeled from the SNOE NO data was multiplied with the three hours of assumed auroral production of the observed amount of NO.

In Paper I the focus for the comparisons was the variation of NO density at higher latitudes, and changes of the total energy deposition from the auroral electrons. In Paper II, however, the amplitude of these variations was important. Some simplifications were done in Paper I when deriving the electron energy from the total time-integrated X-ray data. In this second study, the time-integration was divided in 100 minute intervals, which was approximately the time between each SNOE orbit. The electron energy spectra were derived for each of these intervals, and the total energy input was obtained by summing up these 100 minute electron spectra. This way the variation in the viewing angle for the different regions, was taken into consideration. The auroral electrons for quite different local time sectors were thus not bunched together in one energy spectrum.

The uncertainties of the X-ray spectrum adjustments were difficult to obtain by manual validation of the fitting, since there were that many spectra. The routine for finding a suitable spectrum for the X-ray measurements were made so that the fitting was either double or single exponential (a four or a two parameter spectrum). If the count rates from PIXIE were very low, no spectrum was obtained. And the higher the count rates, the better the spectral adjustments were. To get a measure for the uncertainty of the spectrum fitting of the PIXIE data, the energy flux (for 4<E<100 keV) derived from only single exponential spectra were compared to that derived from only double exponential ones. The cases where more than two spectra were used to provide the energy flux for a geographical box, the difference between the single flux and the double flux was between 16% and 24%. For the few cases where only one or two spectra were used, the average difference for all geographical boxes was less than 25%. The double exponential spectra will generally give a larger electron energy flux than the single exponential. There were, however, no connections between the choices of double versus single exponential fitting, and the cases where the PIXIE derived electron flux was much larger than that from SNOE model calculations. These cases where the PIXIE result was much larger, the fluxes were derived from three to seven X-ray spectra. The spectra from low activity periods were also included in the time-integrated electron energy flux. These only contributed less than 10% of the calculated energy flux. The uncertainties for change in the viewing angle during the 100 minute average, were less than 20% for the beginning and end of the PIXIE observation interval, and less than 10% for the main part of the PIXIE measurements. The look-up table used for obtaining the corresponding electron energy spectra, have been used in several other studies (e.g. *Østgaard et al.*, 2000, 2001; *Aksnes et al.*, 2004). The method was shown to give a fairly good match to the energy spectra derived from UVI and from DMSP and NOAA measurements (e.g. *Østgaard et al.*, 2000). Figure 4.4 shows the comparisons of total electron energy flux for the separate days, including uncertainties of the methods. The combined uncertainty for the energy flux from the NO_x model and SNOE data, was 32%. The total uncertainty for the PIXIE derived energy flux was 27%. Nearly all the cases where the comparisons, including the uncertainties, did not overlap

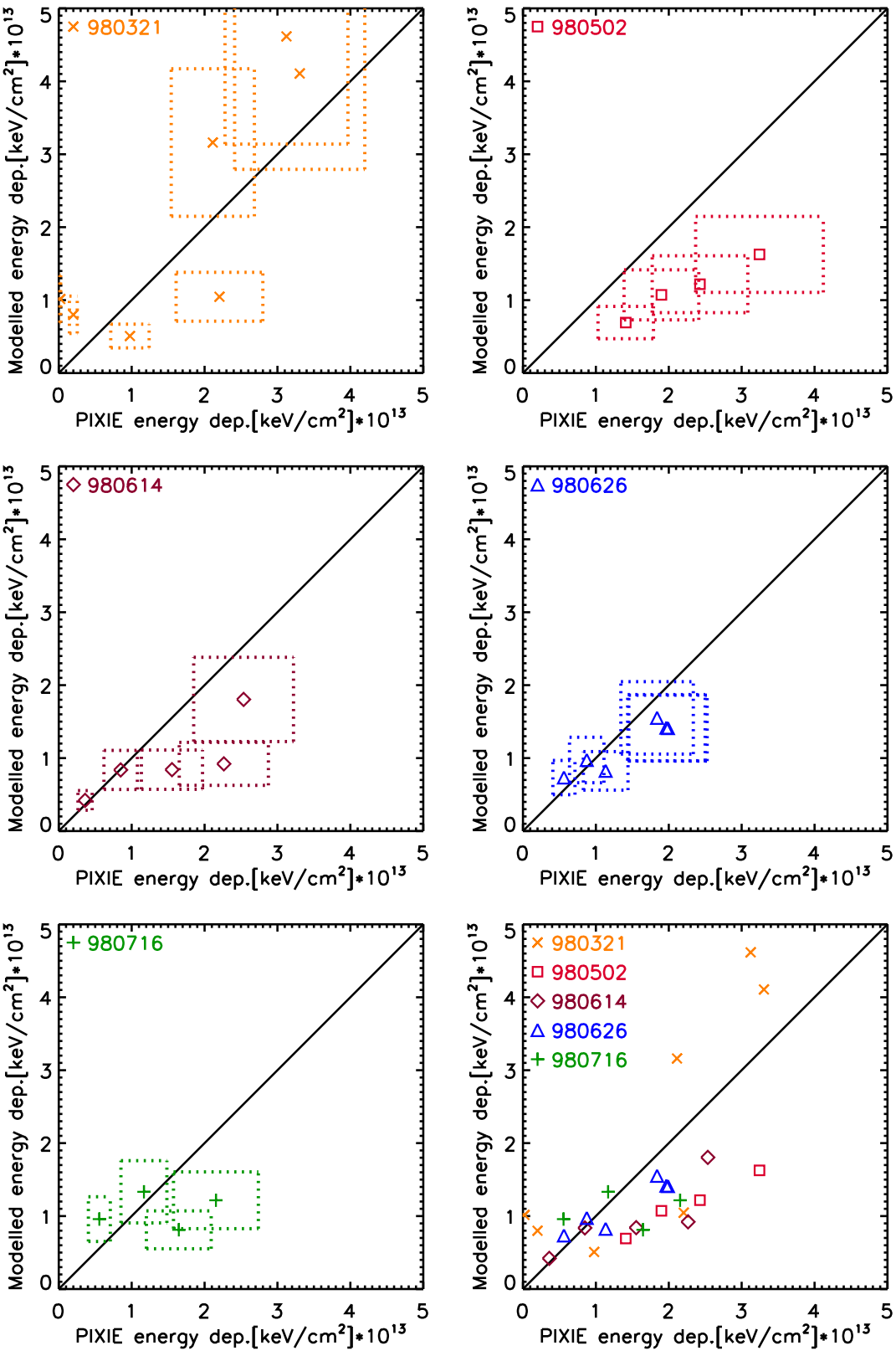

Figure 4.4: Total electron energy deposition (4-100 keV) averaged over the latitude interval covered by the measurements. The five days investigated in Paper II are shown, with the total uncertainty both of the datasets and methods. In the lower right plot all the days are gathered, and this is the color version of Figure 5 of Paper II.

the line of equality, the PIXIE derived energy fluxes were larger.

The result of Paper II showed a tendency that the PIXIE derived electron energy flux was somewhat larger than that derived by the NO_x photochemical model and the SNOE nitric oxide data. This difference was largest for the highest latitudes. The neutral wind effects were not included in the NO_x model calculations. The discrepancies between the NO_x model and the bremsstrahlung method for deriving the auroral electron energy flux, might be related to the simplifications done in the model. The main simplifications were a fixed characteristic energy, a fixed local time interval of precipitation, and one specific altitude for adjustment of model calculation to the SNOE nitric oxide profile. Considering these assumptions the results from Paper II gave confidence that the physical and chemical processes for nitric oxide at higher latitudes were fairly well understood. The difficulty is to get the proper auroral input, both temporal and spatial, for the photochemical model. This was the issue for Paper III. In this following paper it was shown that the background neutral atmosphere invoked in the model, is difficult to estimate by use of an empirical model, like the MSIS models, when there is significant Joule heating. Loss processes that were not included in the photochemical model, like transport effects due to atmospheric heating, can explain the underestimate of electron energy deposition from the model with SNOE nitric oxide density as input parameter.

4.3 Paper III: Thermospheric nitric oxide at higher latitudes - Model calculations with auroral energy input

The third paper addressed the problems of a limited data set for the electron precipitation. Here the continuous electron energy parameters were used as input to the photochemical model for nitric oxide. The output of the model was then compared to the NO density measured by SNOE.

The auroral electron precipitation was from a combination of the electron energy spectra derived from UVI and PIXIE measurements. When including the UVI measurements, one obtains the electron energy parameters in an energy range 1-100 keV. The auroral observations were divided in 10 minute time steps, and the electron energy parameters were derived for each of these time-intervals in a geographical grid of box size 5° latitude times 24° longitude. The electron energy flux from the UVI measurements was based on the intensity of the LBHl emissions, and the mean energy of the electrons were found from the ratio between the LBHl and LBHs emissions. This is described more thoroughly in Chapter 3. The PIXIE derived electron energy spectra were found by use of a look-up table, relating the energy distribution of the auroral electrons to the energy spectra of the bremsstrahlung they produce when they are slowed down in the atmosphere (see Chapter 3). The energy spectra for the X-rays were fitted to the measurements, arranged in six energy channels, for each 10 minute interval. The electron precipitation was assumed to stay constant within this time-interval. The data routine for the photochemical model is based on a maxwellian electron distribution as input parameter (*Bailey et al.*, 2002). Thus

the final 10-minute electron spectrum was represented by a maxwellian energy distribution, with the same integrated energy flux as the combined electron exponential energy spectra from UVI and PIXIE. Since the background atmosphere, modeled by NRLMSISE-00, had a limited time-resolution, the energy input to the photochemical model from the auroral electrons (mW m^{-2}) were averaged over one hour intervals.

To get the continuous auroral energy input, a parametrization of geomagnetic disturbances was used. This involved geomagnetic ground data from the SuperMAG database, segmented in 24° geographic longitude intervals. To find if there was any significant correlation between the precipitating electrons and the maximum negative deflection in the north component of the ground magnetic field, the magnetometer data were compared to the UVI and PIXIE derived electron energy fluxes within the 24° longitude sectors. The data from UVI/PIXIE were averaged over the latitude interval between 50°N and 70°N. The comparisons were done for four days in 1998 (120, 122, 123, and 177), with both high and low auroral activity. The correlation between hourly averages of the maximum negative deflection of the north component of the geomagnetic field, and the hourly averaged electron energy flux was 0.75. The uncertainties of the comparisons were not small. The calculation of the NO density by the photochemical model depended on long time-intervals of the auroral electron energy input, and the uncertainties of the parametrization were assumed to be more or less levelled out in the calculations. The parametrization was only used in the time-intervals when the UVI and PIXIE measurements did not cover the northern hemisphere.

Thus the new approach of the photochemical model, was to use as input both the energy input from photoelectrons and auroral electrons. The electron energy fluxes and mean energies in one hour intervals from UVI and PIXIE measurements, plus parametrization of the energy flux from geomagnetic data from SuperMAG, were provided in a geographical

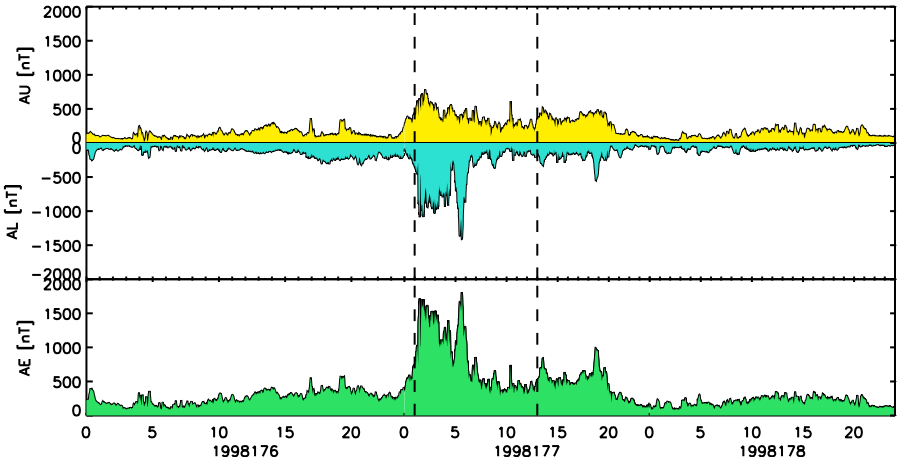

Figure 4.5: AU, AL, and AE indices from the SuperMAG database for day 176 to 178, 1998. The time interval of the UVI and PIXIE measurements are within the dashed vertical lines.

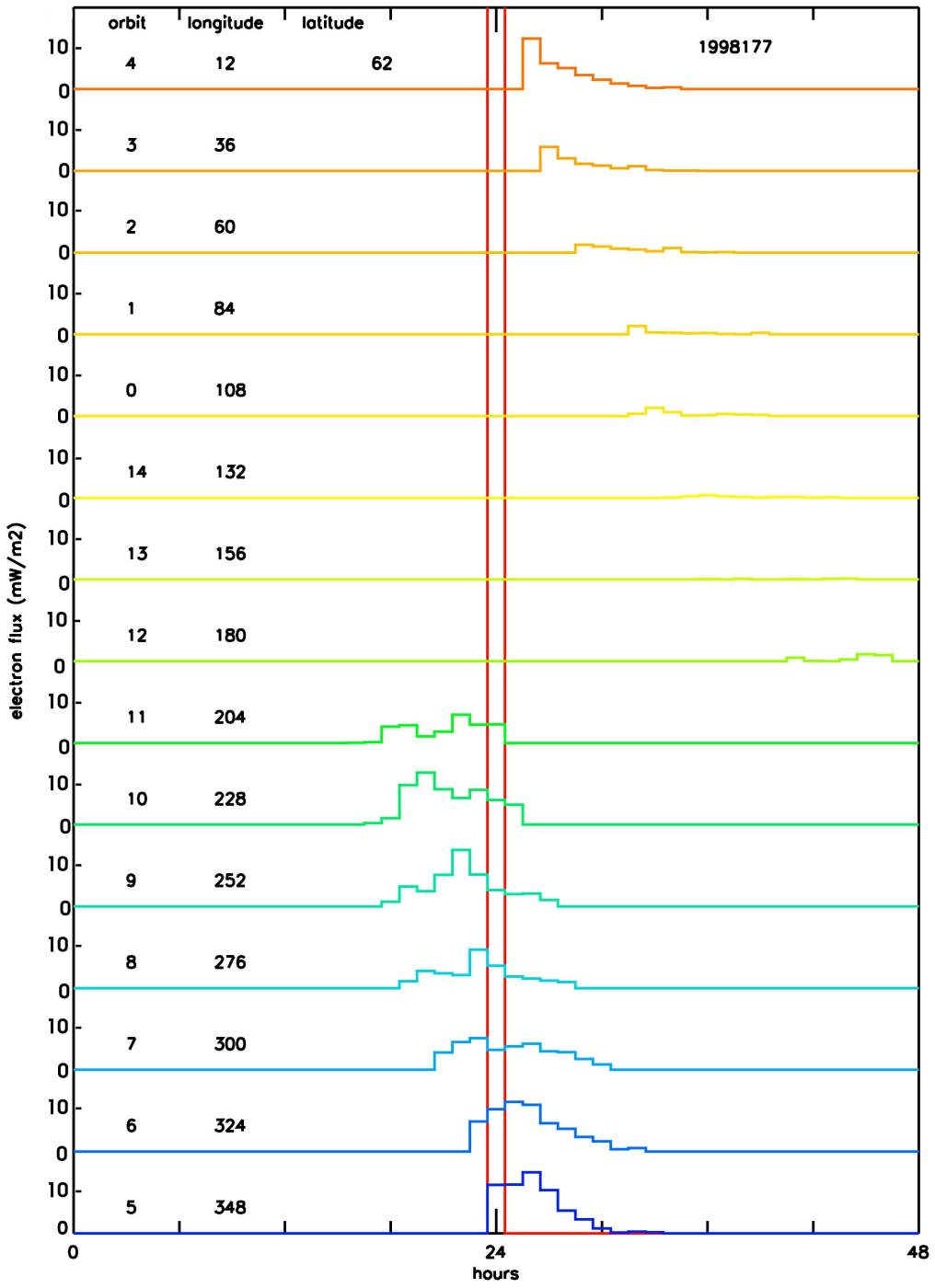

Figure 4.6: The precipitating electron energy flux derived from UVI and PIXIE measurements on day 177 of 1998, 60°-65°N. The flux is plotted for all the fifteen longitude sectors, as a function of solar local time for each of the regions.

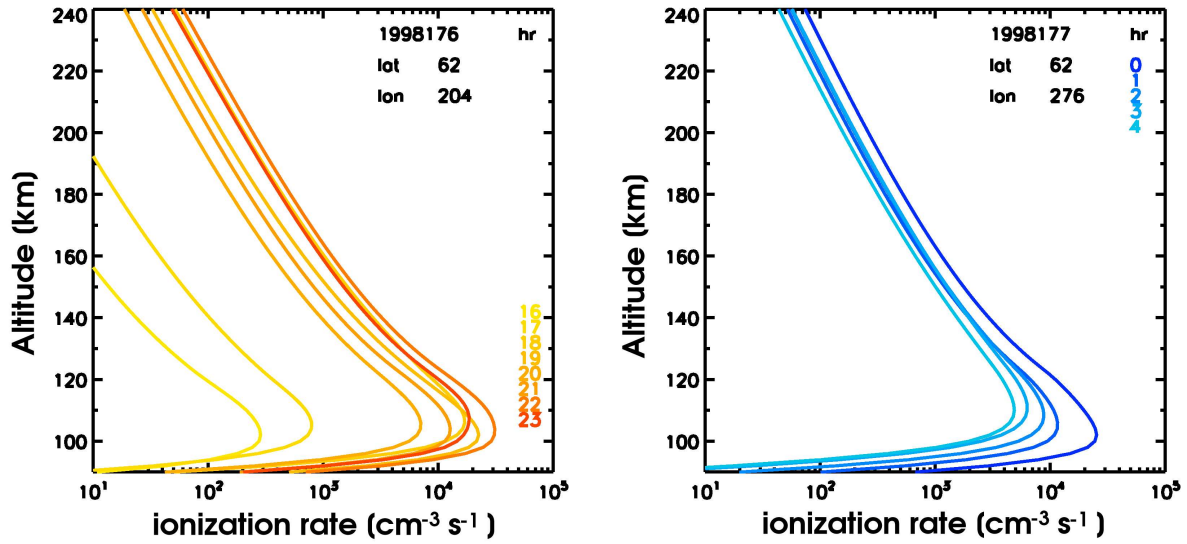

Figure 4.7: The total ionization rates [ionizations/ cm^3 sec] as function of altitude [km]. Calculated by the photochemical model with the auroral electron energy input from UVI and PIXIE measurements. The different colors represents the different solar local hours for the regions. Day 176-177 of 1998, 60°-65°N, and 192°-216°E (left) and 264°-288°E (right).

grid. Also the model atmosphere conditions from NRLMSISE-00 were for the local time of each longitude sector. Previously the model atmosphere conditions at 0000 UT were always used.

In addition to the storm event presented in Paper III, a more isolated event of day 177, 1998, was investigated. For this comparison, only the UVI and PIXIE measurements were used, not the geomagnetic parametrization. Figure 4.5 shows the AU, AL, and AE indices for day 176 to 178, 1998. The onset of the storm was ∼00 UT on day 177. The Dst index for this storm went as low as -100 nT. The UVI and PIXIE measurements were within the time-interval between the dashed lines, covering most of the hours of significant auroral activity. The previous and following day of the event, were rather quiet. The hourly electron energy flux and mean energy were derived from UVI and PIXIE observations, as described above. Figure 4.6 shows the electron energy flux used as input to the model, for different longitude sectors, organized as a function of solar local time for each of the sectors. Left side of the red pillar is day 176. For some of the longitude sectors the auroral activity happening on day 177 in UT hours, are shifted to day 176 in solar local time hours.

From the auroral electron energy input, the ionization rates of N_2, O_2, O, and the dissociation rate of N_2 were calculated. The time variation of these rates follows the time variation of the auroral energy flux. The same rates were calculated from the photoelectrons produced from solar soft X-rays, and the ionization rates were also calculated from the solar FUV spectrum. Figure 4.7 shows two examples of the total ionization rates calculated by the model, with the auroral energy input shown in Figure 4.6. The different colors display the different hours (SLT), listed on the right side of the plots. The altitude profile of the

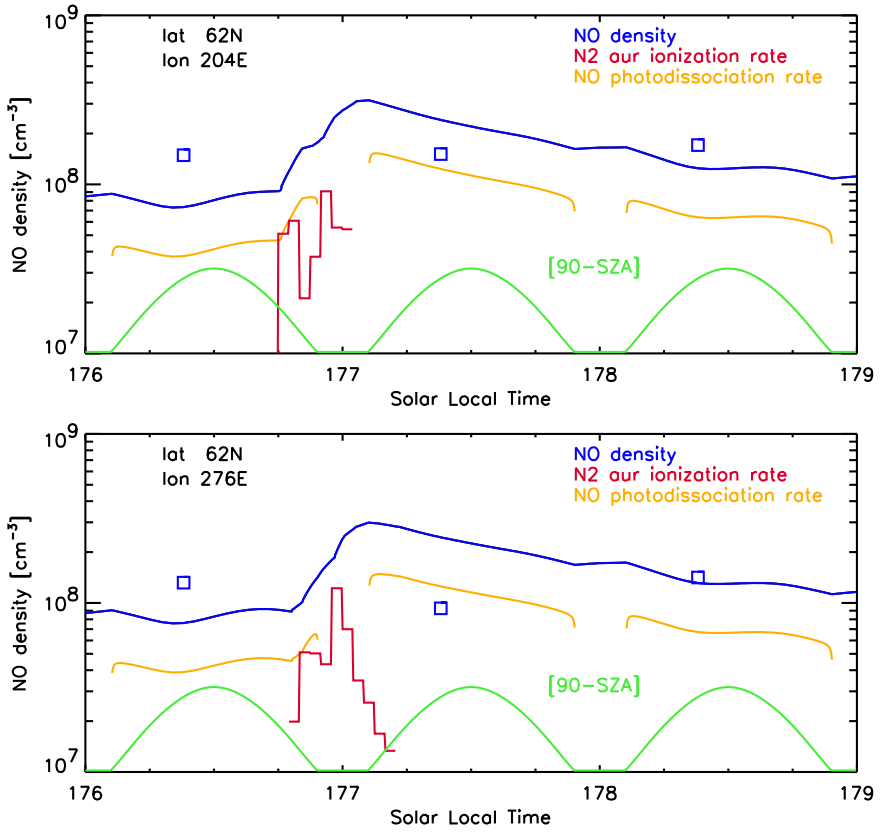

Figure 4.8: Nitric oxide density calculated by the photochemical model at 106 km altitude (blue line) with auroral electron energy input from UVI and PIXIE measurements. The N_2 ionization rate (red, arbitrary scale) is directly proportional to the electron energy input. The blue squares are the NO density at 106 km altitude, measured by SNOE in the specific geographic sectors. The NO photodissociation rate (yellow, arbitrary scale), and the solar elevation angle (green, arbitrary scale), are also shown.

ionization is related to the mean energy of the precipitating electrons. Lower mean energy will give maximum ionization at a higher altitude. The amplitude of the ionization is directly related to the input electron energy flux.

Two examples of the calculated nitric oxide density (blue line) at 106 km altitude for days 176-178, 1998, are shown in Figure 4.8 as a function of solar local time. Also shown is the measured NO density (blue squares) for the particular longitude sectors (one measurement per day, ∼10:30 SLT). On an arbitrary scale, the N_2 auroral ionization rate (red), the NO photodissociation rate (yellow) and the solar elevation angle (green) are plotted. The last is an indication of the length of day at 62.5°N and 106 km altitude. For these two longitude sectors (around 204°E and 276°E), the measured NO density does not show much variation for the three days. In fact, for the lower plot the NO density decreased from day 176 to day 177, even though UVI and PIXIE observed auroral activity in that region during the night. On day 176, the lower modeled density relative to the

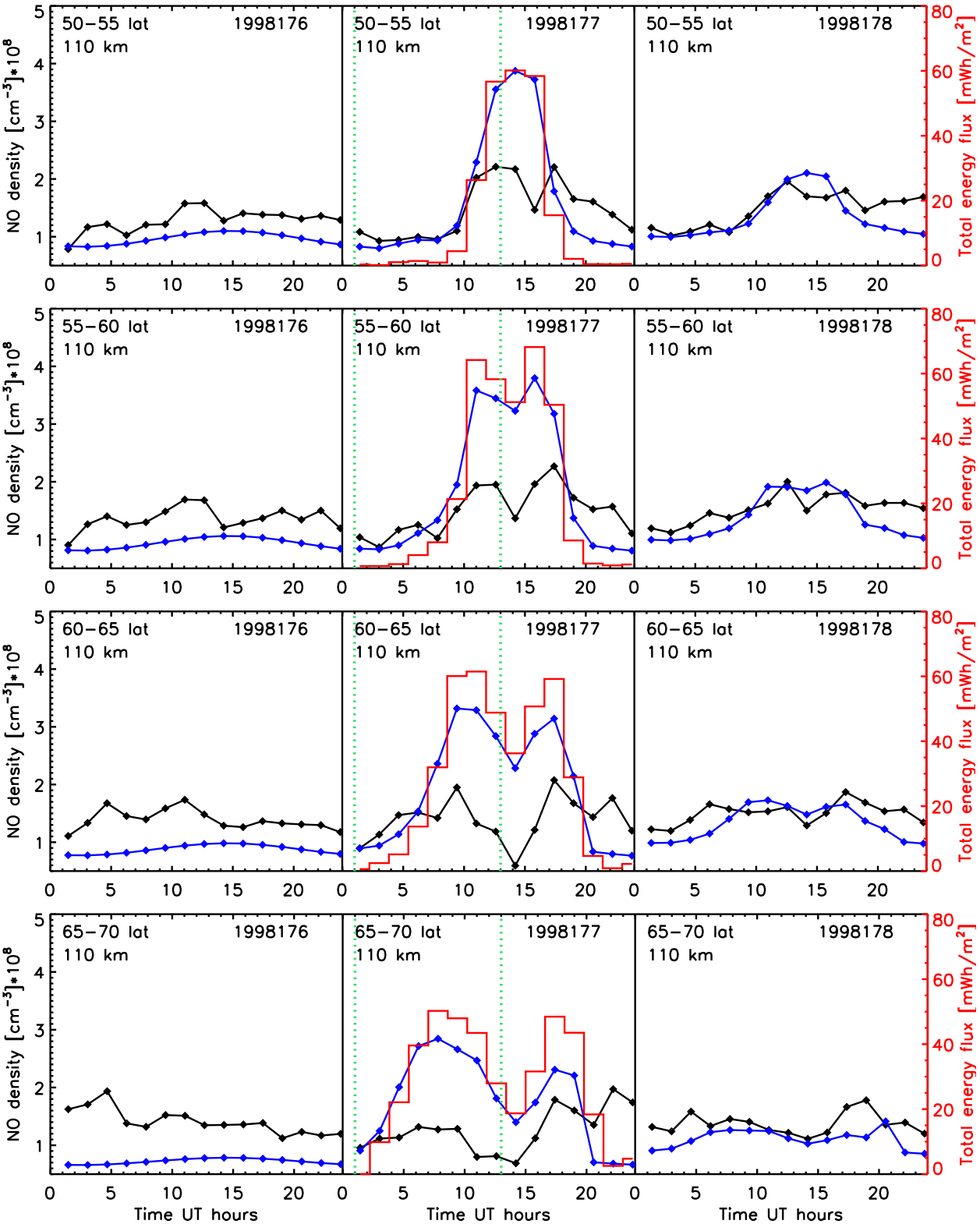

Figure 4.9: The nitric oxide density at 110 km altitude as a function of universal time, day 176 to 178 of 1998, measured by SNOE (black) and modeled (blue). Each of the points are for different longitude sectors. The total electron energy flux derived from the UVI and PIXIE measurements (red) are used as input to the model. The histogram is shifted in time to the respective longitude intervals of the NO density. The time intervals of the auroral measurements are within the green lines.

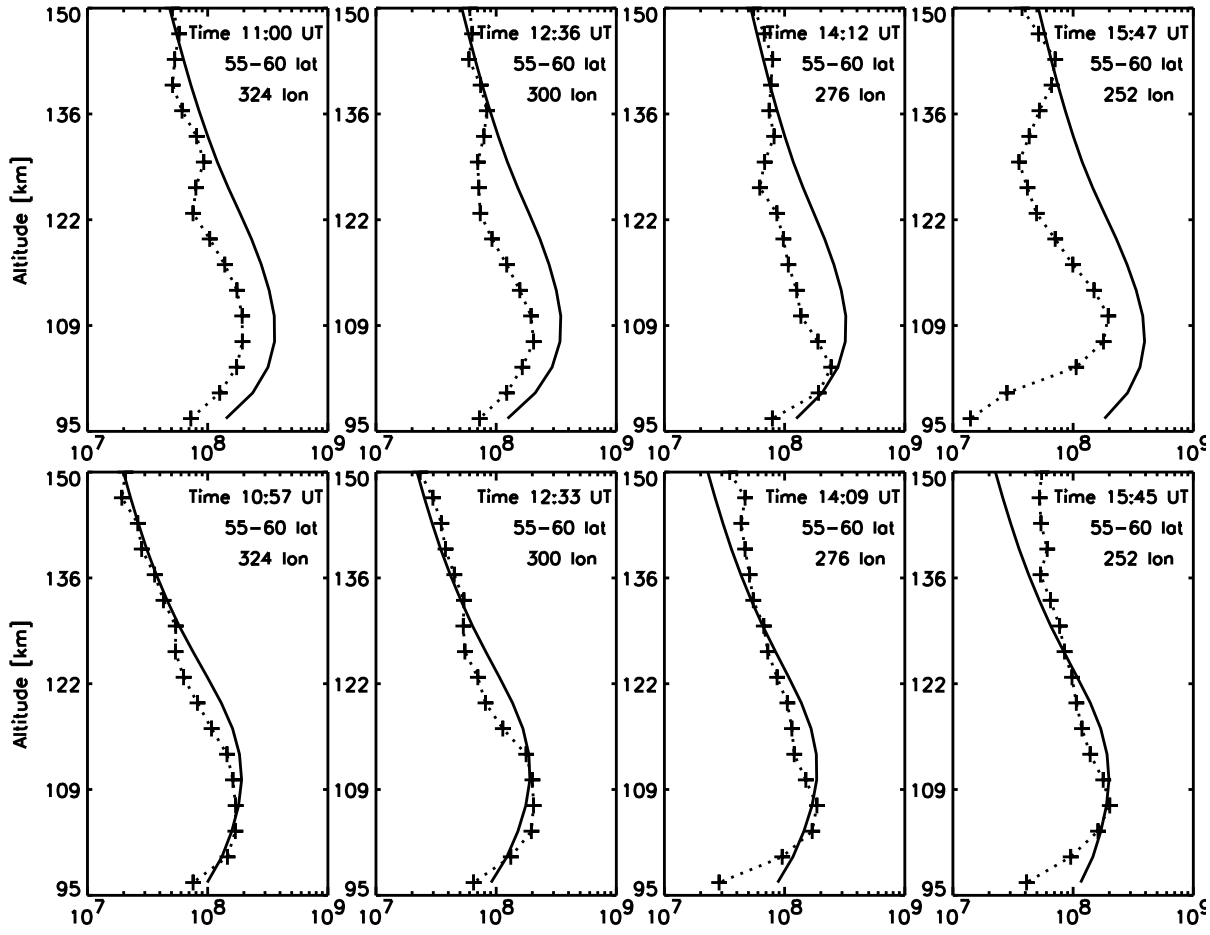

Figure 4.10: NO density 55°-60°N, four longitude regions, as measured by SNOE (dotted with crosses), and calculated from the NO_x model (solid line). The upper four are for day 177, and the lower four are for day 178, 1998. The universal time for the SNOE measurements are given in each of the plot.

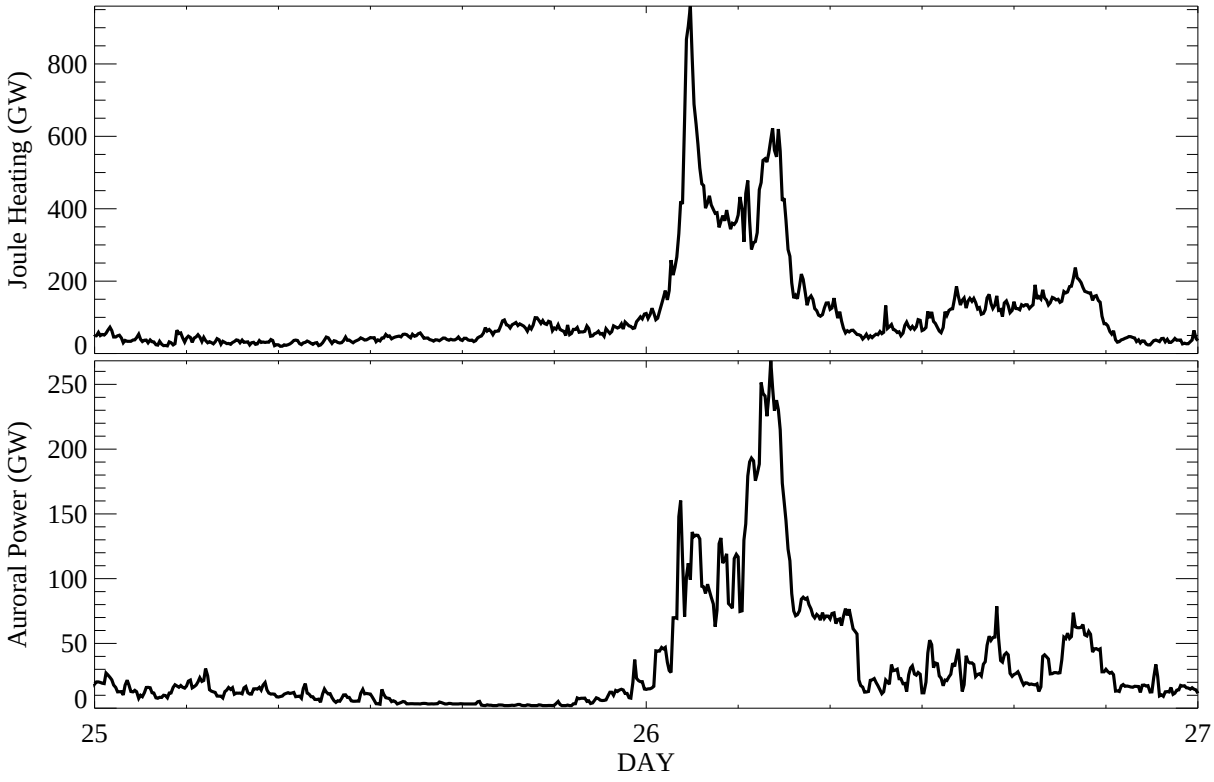

Figure 4.11: Joule heating (top) and auroral power (bottom) from the AMIE model, for day 176 (25 June) and 177 (26 June) of 1998.

measured, is probably due to lack of measurements of the auroral energy input for day 175-176. The day of the event, 177, the model overestimates the NO density. For the day after the storm, 178, when the background atmosphere had settled down, the agreement between the model and the measurements is quite good.

Figure 4.9 shows the calculated (blue) and measured (black) NO density at 110 km altitude for latitudes from 50°N (top) to 70°N (bottom), as a function of universal time from day 176 to day 178. Also shown is the total electron energy flux (red) for the different longitude sectors. These are integrated over time, from the start of the UVI and PIXIE measurements to the time of the different SNOE orbits. The histogram of the energy flux is shifted in time to fit the corresponding NO longitude box. Note that each of the marked points on the NO density curves are different longitude sectors, 24° apart. The green lines indicate the time-interval (UT) of the UVI and PIXIE measurements. On day 176 the modeled NO density is quite low, as mentioned above. The day of the event, 177, the model and the measurements start out with quite similar values, and then the model greatly exceeds the measurements. At the end of the day, the measurements are again larger than the model. On day 178, the model calculations are much better related to reality. This is also evident from the altitude plots in Figure 4.10, showing the measured (crosses) and the modeled (solid line) NO density as a function of altitude, for 55°-60°N,

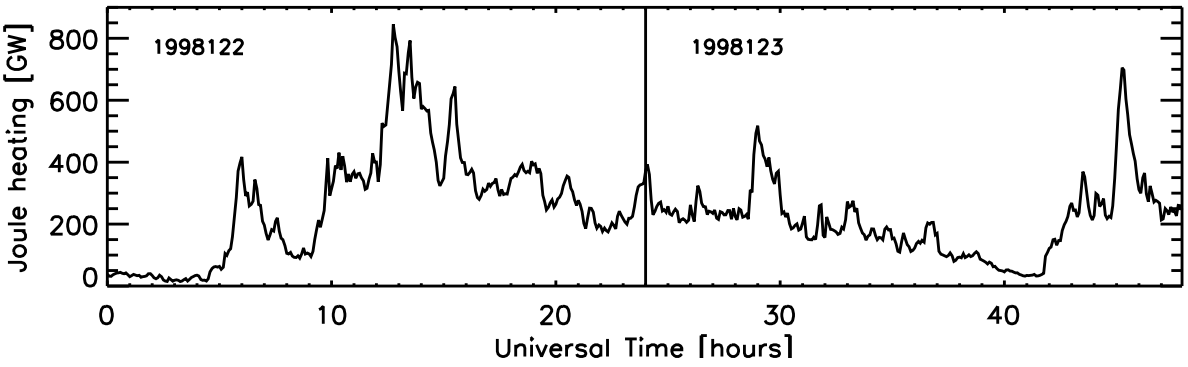

Figure 4.12: Joule heating from the AMIE model, for day 122 and 123 of 1998.

in four different longitude sectors. The UT hours of the SNOE measurements are shown in the upper right corner of each plot. The upper four plots are for day 177. As one can see, the model and the measurements agree at the highest altitudes, but are quite different around the altitude of maximum densities. The next day (178) shown in the lower four plots, the model calculations are in a much better agreement with the measurements for all altitudes.

The comparisons for the May event of 1998, presented in Paper III, show very much the same structure as this event on day 177, 1998. The day of the storm, 122, the modeled nitric oxide density is more than a factor 2 larger than the measured density. The day after the storm, the model is still giving somewhat higher values than the measurements. However, the agreement is highly improved at all altitudes. For the May event, which lasted over several days, the electron energy input to the model was continuous in time for all the days, as described in the beginning of the section.

Figure 4.11 shows the Joule heating (top) and the estimated auroral power (bottom) for days 176 (25 June) and 177 (26 June), 1998, both from the Assimilative Mapping of Ionospheric Electrodynamics (AMIE) procedure (*Richmond*, 1992). As the geomagnetic storm developed on day 177, there was also strong Joule heating. This was also evident for day 122 for the May event. The Joule heating from the AMIE procedure for days 122 and 123, 1998, is shown in Figure 4.12. This storm had a longer recovery than the one for day 177. The Joule heating was significantly larger on day 122 than on day 123. The model for the background atmosphere, NRLMSISE-00, used in the photochemical model calculations for the nitric oxide density, is based on a hydrostatic model (*Bates*, 1959). When the atmosphere undergoes strong heating, and the expansions that invokes, the atmosphere may not be in hydrostatic balance (*Burns et al.*, 2006). Although the NRLMSISE-00 model uses 3 hour geomagnetic Ap index as input parameter, this is not sufficient to estimate the changes of the atmosphere during the geomagnetic storm when the Joule heating is considerable.

The conclusion of Paper III was that the photochemical NO_x model is able to calculate the chemical effects of the nitric oxide density in the lower thermosphere as a result of auroral electron precipitation. This is based on the good agreement between the modeled

nitric oxide density and the density measured by SNOE the days after the geomagnetic storms, when the background atmosphere had settled down. The disagreement between the model and the measurements for the day of the storm onset, is thought to be due to the disruption of the atmosphere due to significant Joule heating. Loss effects due to increased neutral transport away from the production area, are not included in the model. It would be better to use a three dimensional global circulation model for the background atmosphere, instead of the empirical NRLMSISE-00 model.

The three papers have answered questions regarding the temporal variations of nitric oxide density in the auroral regions. Instead of using daily average values, the time-history of the auroral intensity for the specific regions of the nitric oxide measurements were investigated. The variations of nitric oxide density in the lower thermosphere with the accumulated auroral X-ray intensity have been confirmed in Paper I. The understanding of the chemical processes producing and destroying nitric oxide in the lower thermosphere during a geomagnetic storm, was tested in Papers II and III. These results indicate that while the chemical processes are probably well understood, the processes related to transport of neutral constituents are more difficult to incorporate.

Bibliography

Acuña, M. H., K. W. Ogilvie, D. N. Baker, S. A. Curtis, D. H. Fairfield, and W. H. Mish (1995), The global geospace science program and its investigations, *Space Science Reviews*, *71*, 5.

Ahn, B. H., S.-I. Akasofu, and Y. Kamide (1983), The Joule heat production rate and the particle energy injection rate as a function of the geomagnetic indices AE and AL, *J. Geophys. Res.*, *88*, 6275.

Ahn, B. H., B. A. Emery, H. W. Kroehl, and Y. Kamide (1999), Climatological characteristics of the auroral ionosphere in terms of electric field and ionospheric conductance, *J. Geophys. Res.*, *104*, 10,031.

Akasofu, S.-I. (1981), Energy coupling between the solar wind and the magnetosphere, *Space Sci. Rev.*, *28*, 121.

Aksnes, A., J. Stadsnes, G. Lu, N. Østgaard, R. R. Vondrak, D. L. Detrick, T. J. Rosenberg, G. A. Germany, and M. Schulz (2004), Effects of energetic electrons on the electrodynamics in the ionosphere, *Ann. Geophysicae*, *22*, 475.

Anderson, P. C., D. L. Chenette, D. L. McKenzie, J. M. Quinn, M. Grande, and M. Carter (1998), Energetic auroral electron distribution derived from global x-ray measurements and comparison with in-situ particle measurements, *Geophys. Res. Lett.*, *25*, 4105.

Bailey, S. M., T. N. Woods, C. A. Barth, S. C. Solomon, L. R. Canfield, and R. Korde (2000), Measurements of the solar soft x-ray irradiance by the Student Nitric Oxide Explorer: First analysis and underflight calibrations, *J. Geophys. Res.*, *105*, 27,179.

Bailey, S. M., C. A. Barth, and S. C. Solomon (2002), A model of nitric oxide in the lower thermosphere, *J. Geophys. Res.*, *107*, 1206.

Baker, D. N., C. A. Barth, K. E. Mankoff, S. G. Kanekal, S. M. Bailey, G. M. Mason, and J. E. Mazur (2001), Relationships between precipitating auroral zone electrons and lower thermospheric nitric oxide densities: 1998-2000, *J. Geophys. Res.*, *106*, 24,465.

Banks, P. M., and A. F. Nagy (1970), Concerning the influence of elastic scattering upon photoelectron transport and escape, *J. Geophys. Res.*, *75*, 1902.

Barth, C. (1992), Nitric oxide in the lower thermosphere, *Planet. Space Sci.*, *40*, 315.

Barth, C. (1995), Nitric oxide in the lower thermosphere, *Geophysical Monograph*, *87*, 225.

Barth, C. A., and S. M. Bailey (2004), Comparison of a thermospheric photochemical model with Student Nitric Oxide Explorer (SNOE) observations of nitric oxide, *J. Geophys. Res.*, *109*(A03304), doi:10.1029/2003JA010227.

Barth, C. A., and F. G. Eparvier (1993), A method of measuring the temperature of the lower thermosphere, *J. Geophys. Res.*, *98*, 9437.

Barth, C. A., D. W. Rusch, and A. I. Stewart (1973), The UV nitric oxide experiment for Atmosphere Explorer, *Radio Sci.*, *8*, 379.

Barth, C. A., S. M. Bailey, and S. C. Solomon (1999), Solar-terrestrial coupling: Solar soft x-rays and thermospheric nitric oxide, *Geophys. Res. Lett.*, *26*, 1251.

Barth, C. A., K. D. Mankoff, S. M. Bailey, and S. C. Solomon (2003), Global observations of nitric oxide in the thermosphere, *J. Geophys. Res.*, *108*, 1027.

Barth, C. A., D. N. Baker, and S. M. Bailey (2004), Seasonal variation of auroral electron precipitation, *Geophys. Res. Lett.*, *31*, doi:10.1029/2003GL018892.

Bates, D. R. (1959), Some problems concerning the terrestrial atmosphere above about the 100 km level, *Proc. R. Soc. London*, *253*(Ser. A), 451.

Belitza, D. (1986), International reference ionosphere: Recent developments, *Radio Sci.*, *21*, 343.

Berger, M. J., and S. Seltzer (1972), Bremsstrahlung in the atmosphere, *J.Atmos. Terr. Phys.*, *34*, 85–108.

Brekke, A., S. Nozawa, and T. Sparr (1994), Studies of the E-region neutral wind in the quiet auroral ionosphere, *J. Geophys. Res.*, *99*, 8801–8825.

Burns, A. G., W. Wang, T. L. Killeen, S. C. Solomon, and M. Wiltberger (2006), Vertical variations in the N_2 mass mixing ratio during a thermospheric storm that have been simulated using a coupled magnetosphere-ionosphere-thermosphere model, *J. Geophys. Res.*, *111*(A11309), doi:10.1029/2006JA011746.

Callis, L. B., M. Natarajan, and J. D. Lambeth (2001), Solar-atmospheric coupling by electrons (SOLACE): 3. Comparisons of simulations and observations, 1979-1997, issues and implications, *J. Geophys. Res.*, *106*, 7523.

Cleary, R. J. (1986), Daytime high-latitude rocket observations of the NO γ, δ and ε bands, *J. Geophys. Res.*, *91*, 11,337.

Codrescu, M. V., T. J. Fuller-Rowell, R. G. Roble, and D. S. Evans (1997), Medium energy particle precipitation influences on the mesosphere and lower thermosphere, *J. Geophys. Res.*, *102*, 19,977.

Codrescu, M. V., T. J. Fuller-Rowell, J. C. Foster, J. M. Holt, and S. J. Cariglia (2000), Electric field variability associated with the Millstone Hill electric field model, *J. Geophys. Res.*, *105*, 5265.

Cravens, T. E., and A. I. Stewart (1978), Global morphology of nitric oxide in the lower E-region, *J. Geophys. Res.*, *83*, 2446.

Cravens, T. E., J.-C. Gerard, M. LeCompte, A. I. Stewart, and D. W. Rusch (1985), The global distribution of nitric oxide in the thermosphere as determined by the Atmosphere Explorer D satellite, *J. Geophys. Res.*, *90*, 9862.

Dobbin, A. L., A. D. Aylward, and M. J. Harris (2006), Three-dimensional GCM modeling of nitric oxide in the lower thermosphere, *J. Geophys. Res.*, *111*, doi: 10.1029/2005JA011543.

Eparvier, F. G., and C. A. Barth (1992), Self-absorption theory applied to rocket measurements of the nitric oxide (1,0) γ band in the daytime thermosphere, *J. Geophys. Res.*, *97*, 13,723.

Farmer, A. J. D., V. Hasson, and R. W. Nicholls (1972), Absolute oscillator strength measurements of the $(\nu'' = 0, \nu' = 0 - 3)$ bands of the $(A^2\Sigma - X^2\Pi)$ γ-system of nitric oxide, *J. Quant. Spectrosc. Radiat. Transfer*, *12*, 627.

Foster, J. C., J. M. Holt, R. G. Musgrove, and D. S. Evans (1986), Ionospheric convection associated with discrete levels of particle precipitation, *Geophys. Res. Lett.*, *13*, 656.

Fuller-Rowell, T. J., and D. S. Evans (1987), Height-integrated Pedersen and Hall conductivity patterns inferred from the TIROS-NOAA satellite data, *J. Geophys. Res.*, *92*, 7606.

Funke, B., M. Lopez-Puertas, G. Stiller, T. v. Clarmann, and M. Hopfner (2001), A new non-LTE retrieval method for atmospheric parameters from MIPAS-ENVISAT emission spectra, *Adv. Space Res.*, *27*, 1099.

Galand, M., and D. Lummerzheim (2004), Contribution of proton precipitation to space-based auroral FUV observations, *J. Geophys. Res.*, *109*, doi:10.1029/2003JAA010321.

Galand, M., T. J. Fuller-Rowell, and M. V. Codrescu (2001), Response of the upper atmosphere to auroral protons, *J. Geophys. Res.*, *106*, 127.

Garcia, R. R., and S. Solomon (1983), A numerical model of the zonally averaged dynamical and chemical structure of the middle atmosphere, *J. Geophys. Res.*, *88*, 1379.

Gerard, J.-C., and C. A. Barth (1977), High-latitude nitric oxide in the lower thermosphere, *J. Geophys. Res.*, *82*, 674.

Germany, G. A., G. K. Parks, M. J. Brittnacher, J. Cumnock, D. Lummerzheim, J. F. Spann, L. Chen, P. G. Richards, and F. J. Rich (1997), Remote determination of auroral energy characteristics during substorm activity, *Geophys. Res. Lett.*, *24*, 995.

Germany, G. A., G. K. Parks, M. J. Brittnacher, J. F. Spann, J. Cumnock, D. Lummerzheim, F. J. Rich, and P. G. Richards (1998a), Energy characterization of a dynamic auroral event using GGS UVI images, in *Geospace Mass and Energy Flow: Results From the International Solar-Terrestrial Physic Program*, edited by J. L. Horwitz, D. L. Gallagher, and W. K. Peterson, Geophys. Monogr. Ser., p. 143, AGU, Washington, D. C.

Germany, G. A., J. F. Spann, G. K. Parks, M. J. Brittnacher, R. Elsen, L. Chen, D. Lummerzheim, and M. H. Rees (1998b), Auroral observations from the Polar Ultraviolet Imager (UVI), in *Geospace Mass and Energy Flow: Results From the International Solar-Terrestrial Physic Program*, edited by J. L. Horwitz, D. L. Gallagher, and W. K. Peterson, Geophys. Monogr. Ser., p. 149, AGU, Washington, D. C.

Gjerloev, J. W., and R. A. Hoffman (2000), Height integrated conductivity in auroral substorms, 2. Modeling, *J. Geophys. Res.*, *105*, 227.

Gjerloev, J. W., and R. A. Hoffmann (2001), The convection electric field in auroral substorms, *J. Geophys. Res.*, *106*, 12,919.

Gjerloev, J. W., M. Friel, R. A. Hoffman, K. Takahashi, R. Barnes, C. Meng, and R. A. Greenwald (2004), The global magnetometer network initiative: SuperMAG, *Eos Trans. AGU, 85(47), Fall Meet. Suppl., Abstract SH41A-1079.*

Gussenhoven, M. S., D. A. Hardy, and W. J. Burke (1981), DMSP/F2 Electron observations of equatorward auroral boundaries and their relationship to magnetic electric fields, *J. Geophys. Res.*, *86*, 768.

Gussenhoven, M. S., D. A. Hardy, and N. Heinemann (1983), Systematics of the equatorward diffuse auroral boundary, *J. Geophys. Res.*, *88*, 5692.

Hardy, D. A., M. S. Gussenhoven, and E. Holeman (1985), A statistical model of auroral electron precipitation, *J. Geophys. Res.*, *90*, 4229.

Hays, P. B., R. A. Jones, and M. H. Rees (1973), Auroral heating and the composition of the neutral atmosphere, *Planet. Space Sci.*, *21*, 559.

Hedin, A. E. (1983), A revised thermospheric model based on mass-spectrometer and incoherent scatter data - MSIS-83, *J. Geophys. Res.*, *88*, 170.

Hedin, A. E. (1991), Extension of the MSIS thermosphere model into the middle and lower atmosphere, *J. Geophys. Res.*, *96*, 1159.

Hinteregger, H. E., K. Fukui, and B. R. Gilson (1981), Observational, reference, and model data on solar EUV, from measurements on AE-E, *Geophys. Res. Lett.*, *8*, 1147.

Imhof, W. L., et al. (1995), The Polar Ionospheric X-ray Imaging Experiment (PIXIE), *Space Sci. Rev.*, *71*, 385.

Kamide, Y., and S. Kokubun (1996), Two-component auroral electrojet: Importance for substorm studies, *J. Geophys. Res.*, *101*, 13,027.

Killeen, T. L., et al. (1988), On the relationship between the dynamics of the polar thermosphere and the morphology of the visible aurora: Global-scale observations from Dynamics Explorers -1 and -2, *J. Geophys. Res.*, *93*, 2675.

Langhoff, S. R., J. C. W. Bauschlicher, and H. Partridge (1988), Theoretical study of the NO γ system, *J. Chem. Phys.*, *89*, 4909.

Lorence, L. J. (1992), CEPXS/ONELD version 2.0: A discrete ordinates code package for general one-dimensional coupled electron-photon transport, *IEEE Trans. Nuclear Science*, *39*(4), 1031.

Lu, G., et al. (1998), Global energy deposition during the January 1997 magnetic cloud event, *J. Geophys. Res.*, *103*, 11,685.

Marsh, D. R., S. C. Solomon, and A. E. Reynolds (2004), Empirical model of nitric oxide in the lower thermosphere, *J. Geophys. Res.*, *109*, doi:10.1029/2003JA010199.

McCoy, R. P. (1983), Thermospheric odd nitrogen: 1. NO, N(^{4}S), O(^{3}P) densities from rocket measurements of the NO δ and γ bands and the O_2 Herzberg I bands, *J. Geophys. Res.*, *88*, 3197.

Merkel, A. W., C. A. Barth, and S. M. Bailey (2001), Altitude determination of ultraviolet measurements made by the Student Nitric Oxide Explorer, *J. Geophys. Res.*, *106*, 30,283.

Minschwaner, K., and D. E. Siskind (1993), A new calculation of nitric oxide photolysis in the stratosphere, mesosphere, and lower thermosphere, *J. Geophys. Res.*, *98*, 20,401.

Østgaard, N., J. Bjordal, J. Stadsnes, and E. Thorsen (1999), PIXIE data processing at the University of Bergen. Tecnical report, *Tech. Rep. 1999-05*, Dept. of Physics, University of Bergen, Bergen, Norway.

Østgaard, N., J. Stadsnes, J. Bjordal, R. R. Vondrak, S. A. Cummer, D. L. Chenette, M. Schulz, and J. G. Pronko (2000), Cause of the localized maximum of x-ray emission in the morning sector: A comparison with electron measurements, *J. Geophys. Res.*, *105*, 20,869.

Østgaard, N., J. Stadsnes, J. Bjordal, G. A. Germany, R. R. Vondrak, G. K. Parks, S. A. Cummer, D. L. Chenette, and J. G. Pronko (2001), Auroral electron distributions derived from combined UV and X-ray emissions, *J. Geophys. Res.*, *106*, 26,081.

Østgaard, N., R. R. Vondrak, J. W. Gjerloev, and G. Germany (2002), A relation between the energy deposition by electron precipitation and geomagnetic indices during substorms, *J. Geophys. Res.*, *107*(A9), 1246, doi:10.1029/2001JA002003.

Petrinec, S. M., W. L. Imhof, C. A. Barth, K. D. Mankoff, D. N. Baker, and J. G. Luhmann (2003), Comparison of thermospheric high-latitude nitric oxide observations from SNOE and global auroral X-ray bremsstrahlung observations from PIXIE, *J. Geophys. Res.*, *108*, 1123.

Picone, J. M., A. E. Hedin, D. P. Drob, and A. C. Aikin (2002), NRLMSISE-00 empirical model of the atmosphere: Statistical comparisons and scientific issues, *J. Geophys. Res.*, *107*, doi:10.1029/2002JA009430.

Piper, L. G., and L. M. Cowles (1986), Einstein coefficients and transition moment variation for the NO($A^2\Sigma^+ - X^2\Pi$) transition, *J. Chem. Phys.*, *85*, 2419.

Randall, C. E., D. E. Siskind, and R. M. Bevilacqua (2001), Stratospheric NO_x enhancements in the Southern Hemisphere vortex in winter/spring of 2000, *Geophys. Res. Lett.*, *28*, 2385.

Randall, C. E., V. L. Harvey, C. S. Singleton, P. F. Bernath, C. D. Boone, and J. U. Kozyra (2006), Enhanced NO_x in 2006 linked to strong upper stratospheric Arctic vortex, *Geophys. Res. Lett.*, *33*, doi:10.1029/2006GL027160.

Randall, C. E., et al. (2005), Stratospheric effects of energetic particle precipitation in 2003-2004, *Geophys. Res. Lett.*, *32*, doi:10.1029/2004GL022003.

Rees, M. H. (1963), Auroral ionization and exitation by incident energetic electrons, *Planet. Space Sci.*, *11*, 1209.

Rees, M. H. (1989), *Physics and Chemistry of the Upper Atmosphere*, Cambridge Univ. Press, Cambridge, UK.

Rees, M. H., and R. G. Roble (1979), The morphology of N and NO in auroral substorm, *Planet. Space Sci.*, *27*, 453.

Richmond, A. D. (1992), Assimilative mapping of ionospheric electrodynamics, *Adv. Space. Res.*, *12*, 59.

Richmond, A. D., E. C. Ridley, and R. G. Roble (1992), A Thermosphere/Ionosphere General Circulation Model with coupled electrodynamics, *Geophys. Res. Lett.*, *19*, 601.

Roble, R. G., E. C. Ridley, A. D. Richmond, and R. E. Dickinson (1988), A coupled thermosphere/ionosphere general circulation model, *Geophys. Res. Lett.*, *15*, 1325.

Rottman, G. J., T. N. Woods, and T. P. Sparn (1993), Solar-stellar irradiance comparison experiment, instrument design, and operation, *J. Geophys. Res.*, *98*, 10,667.

Rusch, D. W., and C. A. Barth (1975), Satellite measurements of nitric oxide in the polar region, *J. Geophys. Res.*, *80*, 3719.

Russel, C. T. (Ed.) (1995), *The global geospace mission*, Kluwer Academic Publishers.

Russel, J. M., et al. (1993), The halogen occultation experiment, *J. Geophys. Res.*, *98*, 10,777.

Siskind, D. E., C. A. Barth, D. S. Evans, and R. G. Roble (1989a), The response of thermospheric nitric oxide to an auroral storm: 2. Auroral latitudes, *J. Geophys. Res.*, *94*, 16,899.

Siskind, D. E., C. A. Barth, and R. G. Roble (1989b), The response of thermospheric nitric oxide to an auroral storm: 1. Low and middle latitudes, *J. Geophys. Res.*, *94*, 16,885.

Siskind, D. E., C. A. Barth, and J. M. Russel (1998), A climatology of nitric oxide in the mesosphere and thermosphere, *Adv. Space Res.*, *21*, 1353.

Siskind, D. E., G. E. Nedoluha, C. E. Randall, M. Fromm, and J. M. I. Russell (2000), An assessment of Southern Hemisphere stratospheric NO_x enhancements due to transport from the upper atmosphere, *Geophys. Res. Lett.*, *27*, 329.

Solomon, S. C., and V. J. Abreu (1989), The 630-nm dayglow, *J. Geophys. Res.*, *94*, 6817.

Solomon, S. C., P. B. Hays, and V. J. Abreu (1988), The auroral 6300 å emission: Observations and modeling, *J. Geophys. Res.*, *93*, 9867.

Solomon, S. C., C. A. Barth, M. J. Erikson, R. A. Kohnert, and A. W. Merkel (1996), The Student Nitric Oxide Explorer, *Proc. SPIE*, *2810*, 121.

Solomon, S. C., C. A. Barth, and S. M. Bailey (1999), Auroral production of nitric oxide measured by the SNOE satellite, *Geophys. Res. Lett.*, *26*, 1259.

Solomon, S. C., S. M. Bailey, and T. N. Woods (2001), Effect of solar soft X-rays on the lower ionosphere, *Geophys. Res. Lett.*, *28*, 2149.

Stevens, M. H. (1995), Nitric oxide gamma band fluorescent scattering and selp-absorption: 1, The mesosphere and lower thermosphere, *J. Geophys. Res.*, *100*, 14,735.

Stevens, M. H., R. R. Conway, J. G. Cardon, and J. M. Russel (1997), MAHRSI observations of nitric oxide in the mesosphere and lower thermosphere, *Geophys. Res. Lett.*, *24*, 3213.

Strickland, D. J., and R. R. Meier (1982), *A photoelectron model for the rapid computation of atmospheric excitation rates*, vol. 5004, chap. NRL Memo. Rep., pp. 1–40, Nav. Res. Lab., Washington, D. C.

Strickland, D. J., D. L. Book, T. P. Coffey, and J. A. Fedder (1976), Transport equation techniques for the deposition of auroral electrons, *J. Geophys. Res.*, *81*, 2755.

Torr, M. R., D. G. Torr, and R. A. Ong (1979), Ionization frequencies for major thermospheric constituents as a function of solar cycle 21, *Geophys. Res. Lett.*, *6*, 771.

Torr, M. R., et al. (1995), A far ultraviolet imager for the International Solar-Terrestrial physics mission, *Space Sci. Rev.*, *71*, 329.

VanHoosier, M. E., J.-D. F. Bartoe, G. E. Brueckner, and D. K. Prinz (1988), Absolute solar spectral irradiance 120 nm-400 nm (results from the Solar Ultraviolet Spectral Irradiance Monitor - SUSIM - experiment on board Spacelab 2), *Astrophys. Lett. Commun.*, *27*, 163.

Verronen, P. T., E. Turunen, T. Ulich, and E. Kyrölä (2002), Modeling the effects of the October 1989 solar proton event on mesospheric odd nitrogen using a detailed ion and neutral chemistry model, *Ann. Geophysicae*, *20*, 1967.

Appendix A
List of abbreviations

ACE	Atmospheric Chemistry Experiment
AE	Atmospheric Explorer
AMIE	Assimilative Mapping of Ionospheric Electrodynamics
CMAT	Coupled Middle Atmosphere and Thermosphere
DMSP	Defense Meteorological Satellite Program
EOF	Empirical Orthogonal Function
EUV	Extreme Ultraviolet
FUV	Far Ultraviolet
GPS	Global Positioning System
HALOE	Halogen Occultation Experiment
HPI	Hemispherical Power Input
ISTP	International Solar Terrestrial Physics
LBLl/s	Lyman Birge Hopfield long/short
MAHRSI	Middle Atmosphere High Resolution Spectrograph Investigation
MIPAS	Michelson Interferometer for Passive Atmospheric Sounding
MSIS	Mass Spectrometer and Incoherent Scatter radar data
NCAR	National Center for Atmospheric Research
NO	Nitric Oxide
NOAA	National Oceanic and Atmospheric Administration
NOEM	Nitric Oxide Empirical Model
NRLMSISE-00	NRL Mass Spectrometer, Incoherent Scatter Radar Extended Model
OGO	Orbiting Geophysical Observatory
PIXIE	Polar Ionospheric X-ray Imaging Experiment
SAMPEX	Solar Anomalous and Magnetospheric Particle Explorer
SLT	Solar Local Time
SME	Solar Mesosphere Explorer
SNOE	Student Nitric Oxide Explorer
SOLSTICE	Solar-Stellar Irradiance Comparison Experiment
SXP	Solar X-ray Photometer
TGCM	Thermospheric General Circulation Model

UARS	Upper Atmosphere Research Satellite
UT	Universal Time
UV	Ultraviolet
UVI	Ultraviolet Imager
UVS	Ultraviolet Spectrometer
3-D	Three dimensional

Appendix B
Glossary

AE index	*Geomagnetic index of the variations of the auroral electrojet current systems*
Ap index	*3-hourly planetary geomagnetic index.*
bremsstrahlung	*X-ray emissions when an electron is slowed down in the coulomb field of a nucleus*
chi-square test	*Test if an observed distribution conforms to any other distribution*
D-region	*Ionosphere layer between ∼50 and 90 km altitude*
Dst index	*Geomagnetic index of the variations of the equatorial ring current*
E-region	*Ionosphere layer between ∼90 and 140 km altitude*
exobase	*The top of the thermosphere, the level at which a large fraction of atmospheric atoms and molecules can leave the atmosphere without colliding with another atom or molecule (those with sufficient speed will escape from the atmosphere)*
F-region	*Ionosphere layer between ∼140 and 1500 km altitude*
g-factor	*A measure of the possibility of absorption of solar radiation at a wavelength, and the subsequent possibility for fluorescent emission.*
hall currents	*Currents that flow in direction perpendicular to both the electric field and the magnetic field.*
heteronuclear	*A molecule consisting of different elements*
ionosphere	*The region of the atmosphere containing free electrons and ions. Influences radiowave propagation of frequencies <30 MHz.*
Joule heating	*The result of momentum transfer from moving electrons colliding with atoms and molecules*
Kp index	*3-hourly index of geomagnetic activity* *Measure of the deviation of the most disturbed horizontal component of the geomagnetic field. Range from 0 to 9.*
mesosphere	*The region of the atmosphere between ∼50 and ∼90 km altitude where the temperature is decreasing with height*
oscillator strength	*A measure of the intensity of a spectral band*
photochemistry	*Chemical reactions involving photons*

Rayleigh scattering	*Scattering of light by particles which are much smaller than the wavelength of the light*
self-absorption	*Absorption of radiation in the radiation-emitting substance itself*
stratosphere	*The region of the atmosphere between ∼10 and ∼50 km altitude where the temperature is increasing with height*
thermosphere	*The region of the atmosphere between ∼90 and ∼400 km altitude where the temperature is increasing with height*
10.7 cm solar flux	*Indicator of the general level of solar activity*